Structure, phase transformations, and defects of HfO$_2$ and ZrO$_2$ nanoparticles studied by ^{181}Ta and ^{111}Cd perturbed angular correlations, ^{1}H magic-angle spinning NMR, XPS, and x-ray and electron diffraction

M. Forker[*] and P. de la Presa[†]

Helmholtz Institut für Strahlen-und Kernphysik, University of Bonn, Nussallee 14-16, D-53115 Bonn, Germany

W. Hoffbauer

Institut für Anorganische Chemie, University of Bonn, Gerhard-Domagk-Strasse 1, D-53121 Bonn, Germany

S. Schlabach, M. Bruns, and D. V. Szabó

Institut für Materialforschung III, Forschungszentrum Karlsruhe GmbH, P.O. Box 3640, D-76021 Karlsruhe, Germany

Structure, phase transformations, grain growth, and defects of bare and alumina-coated nanoparticles of HfO$_2$ and ZrO$_2$ synthesized in a microwave-plasma process have been investigated by x-ray diffraction (XRD), transmission electron microscopy (TEM), and perturbed angular correlation (PAC) spectroscopy. The PAC technique was used to measure the electric quadrupole interactions (QIs) of the nuclear probes ^{181}Ta and ^{111}Cd in nanocrystalline HfO$_2$ and ZrO$_2$ as a function of temperature. For comparison, the QI of ^{181}Ta in the bulk oxides was determined in the same temperature range 300 K $\leq T \leq$ 1550 K. The oxygen-metal ratio of the as-synthesized particles was determined by x-ray photoelectron spectroscopy to be in the range $1.4 \leq x \leq 1.8$. A hydrate surface layer with a hydrogen content of 5–10 wt %, consisting of chemisorbed hydroxyl groups and organic precursor fragments, was detected by ^{1}H magic-angle spinning NMR. XRD and TEM show that bare n-ZrO$_2$, Al$_2$O$_3$-coated n-ZrO$_2$, and Al$_2$O$_3$-coated n-HfO$_2$ are synthesized in the tetragonal or cubic modification with a particle size $d < 5$ nm, whereas bare n-HfO$_2$ is mainly monoclinic. The grain growth activation enthalpy of bare n-ZrO$_2$ is $Q_A = 32(5)$ kJ/mol. Coating with Al$_2$O$_3$ stabilizes the tetragonal over the monoclinic phase, both in hafnia and zirconia nanoparticles. While TEM micrographs of the native nanoparticles reveal a well-ordered cation sublattice, the observation of a broad QI distribution in the PAC spectra suggests a high degree of disorder of the oxygen sublattice. The gradual transformation of the disordered state and the phase evolution were studied by high-temperature QI measurements. Hafnia nanoparticles persist in the monoclinic (m) phase up to $T \leq$ 1400 K. In coated n-ZrO$_2$/Al$_2$O$_3$, the monoclinic and tetragonal (t) phases coexist over a large temperature range, whereas uncoated, initially tetragonal or cubic (t or c) n-ZrO$_2$ presents a sharp $m \leftrightarrow t$ transition. A "defect" component involving 30%–40% of the probe nuclei appears in the ^{181}Ta PAC spectra of all nanoparticles when these are cooled from high temperatures $T \geq$ 1200 K. The temperature dependence of this component can be reproduced by assuming that Ta impurities in hafnia and zirconia may trap electrons at low temperatures. The observation that the defect component appears only in nanoparticles with diameter $d < 100$ nm suggests that mobile electrons are available only in the surface region of the oxide particles, either from oxygen vacancies (V_O) and/or V_O-hydrogen donors at the interface of the nanoparticles and their hydrate layers. This conclusion is supported by the absence of a size effect for ^{111}Cd probes in HfO$_2$ and ZrO$_2$. The temperature dependence of the ^{181}Ta defect fraction is consistent with a Ta$^+$ impurity level at $E_d \sim 0.9$ and 0.6 eV below the hafnia and zirconia conduction band, respectively.

I. INTRODUCTION

Measurements of the electric quadrupole interaction (QI) between a nuclear quadrupole moment Q and an electric field gradient (EFG) at the nuclear site have successfully contributed to numerous areas of solid state research. The applications range from studies of local symmetry and coordination to phase identification and the observation of phase transformations. They encompass studies of structure and electronic properties of defects, atomic motion, solid state reactions, and other properties. The EFG reflects the charge distribution surrounding the probe nucleus. As its magnitude decreases rapidly with increasing distance between the charges and the probe nucleus, QI measurements are particularly well suited for the investigation of structures at atomic scale and are,

therefore, increasingly used to obtain information on the local atomic arrangement in the grains and interfaces of nanocrystalline materials. Examples are studies of the structure of nanosized In-O species in ordered porous materials[1] QI studies of grain boundary sites of fcc metals,[2] WGa nanocomposites,[3] and ZnO nanoparticles.[4]

In the present study, we report an investigation of structural properties, phase transformations, and defects of bare and coated HfO$_2$ and ZrO$_2$ nanoparticles by measurements of electric quadrupole interactions. These were carried out with the perturbed angular correlation (PAC) technique using the radioisotopes ^{181}Ta and ^{111}Cd as probe nuclei. The paper presents the continuation of previous ^{181}Ta PAC studies of structural properties and phase transformations of nanocrystalline (n-) ZrO$_2$ produced by different routes of synthesis.[5,6]

Several aspects of these n-ZrO$_2$ results motivate an extension of the QI studies to nanocrystalline HfO$_2$. Among these aspects are the observation of the tetragonal or cubic (t or c) rather than the monoclinic phase in native ZrO$_2$ nanoparticles, the tetragonal-to-monoclinic transformation upon heating, and the stabilization of the metastable tetragonal phase by coating the particles with a second oxide such as Al$_2$O$_3$. Coarse-grained (cg-) HfO$_2$ shows the same phases as cg-ZrO$_2$ (monoclinic, tetragonal, and cubic), with the phase transitions occurring at significantly higher temperatures. Very little information, however, is presently available on similarities and differences of ZrO$_2$ and HfO$_2$ nanoparticles with respect to the phase of the native state, its thermal evolution, and the influence of oxide coating on these properties.

Besides these structural aspects, a major driving force for the present study was the observation of a puzzling particle size effect made in our previous [181]Ta PAC study[6] of nanocrystalline ZrO$_2$: The fraction of probe nuclei in the monoclinic phase was found to suffer a pronounced reversible reduction when the nanoparticles are cooled from high temperatures. In bulk zirconia, a similar loss of the monoclinic fraction is not observed. One possible explanation of these findings involves the formation of a probe-defect complex, which would reduce the fraction of [181]Ta probes with the QI parameters of monoclinic ZrO$_2$. Information on structure and electronic levels of point defects in nanocrystalline zirconia and hafnia are presently of great scientific and technological interest,[7–10] as their high dielectric constant makes these oxides good candidates for the substitution of SiO$_2$ as gate dielectric layers in future submicron electronic devices. For further evidence possibly corroborating the formation of probe-defect complexes and insights into the nature of these defects, the QI of [181]Ta in hafnia and zirconia nanoparticles was studied in great detail as a function of the thermal history. A basis for comparison was established by applying the same temperature programs to commercial coarse-grained oxides. The QI of [181]Ta in cg-ZrO$_2$ and cg-HfO$_2$ has been extensively investigated in the past (Refs. 11 and 12), and the results of different authors for the absolute values and the temperature dependence of the QI parameters ν_q, η, and δ (for details, see Sec. IV B) agree well. Less attention, however, has been paid to the influence of the thermal history on the different components found in the PAC spectra.

The hypothesis of formation of a probe-defect complex to explain the reversible reduction of the monoclinic fraction can be tested by investigating different probe atoms in the same host material. The charge state of the probe atom can be expected to play an important role in the formation of defect complexes which involve the probe atom. Differences in the temperature dependence of the monoclinic fraction for probes with different charge states would, therefore, be an argument in favor of probe-defect complex formation. This consideration has motivated an extension of the PAC study of nanocrystalline oxides from the pentavalent probe atom [181]Ta to the divalent PAC probe [111]Cd.

X-ray diffraction (XRD) and transmission electron microscopy (TEM) were employed as complementary methods to investigate the structure of the native nanoparticles and to study grain growth and phase evolution with temperature. Furthermore, we used ^{1}H magic-angle spinning (MAS)

NMR and x-ray photoelectron spectroscopy (XPS) to characterize the chemical composition of the nanoparticles in the as-synthesized state.

II. NANOPARTICLE SYNTHESIS AND CHEMICAL CHARACTERIZATION OF THE NATIVE STATE

A. Synthesis

The nanosized particles were synthesized using the Karlsruhe microwave-plasma process. This process is a gas phase process suitable for the preparation of both bare and coated particles[13–15] with a narrow particle size distribution.[16] Noncoated and Al$_2$O$_3$-coated hafnia and zirconia nanoparticles were produced starting from butoxide [Hf-t-butoxide, Hf(OC$_4$H$_9$)$_4$; Zr-t-butoxide, Zr(OC$_4$H$_9$)$_4$] and chloride (HfCl$_4$ and ZrCl$_4$) precursors. For the Al$_2$O$_3$ coating, a chloride precursor (AlCl$_3$) was used. In the process, the water-free precursors were evaporated and transformed to oxides using a microwave-plasma discharge and an Ar/20 vol % O$_2$ gas mixture as reaction gas. The coating of single particles is realized by using two plasma stages consecutively. The working pressure was in the range of 5–10 mbar and the temperature in the plasma zones <900 K. The PAC cascade of the probe nucleus [181]Ta is populated by the β^- decay of the radioisotope [181]Hf, which can be produced by thermal neutron capture in stable [180]Hf (see Sec. IV). To introduce [181]Ta into nanocrystalline ZrO$_2$, about 4 at. % of the corresponding Hf compound was added to the Zr precursor.

B. Chemical characterization of the native state by XPS, ^{1}H magic-angle NMR, and thermogravimetric and combustion analysis

XPS was used to obtain information on the oxygen-metal ratio x of noncoated HfO$_x$ and ZrO$_x$ nanoparticles. The measurements were performed in an ESCALAB-5 electron spectrometer (VG Scientific, East Grinstead, UK). The kinetic energy of the electrons was measured by a 150° hemispherical energy analyzer operated in the constant analyzer energy mode using 20 eV pass energy for elemental spectra. The spectra were fitted with one or more Voigt profiles using UNIFIT (Ref. 17) (binding energy uncertainty: +0.2 eV), and Scofield sensitivity factors[18] were applied for quantification. Systematically, the oxygen-metal ratio was smaller than the value $x=2$ for perfect stoichiometry: $1.4 \leq x \leq 1.8$. In spite of some systematic uncertainty due to line broadening by localized electrostatic charge buildup of the nonconducting samples, this indicates a sizable concentration of oxygen vacancies in the surface region of the nanoparticles, in agreement with the pronounced decrease (relative to the bulk material) of the cation-oxygen coordination seen in the extended x-ray absorption fine structure (EXAFS) spectra of nanocrystalline zirconia.[19,20] A similar oxygen-metal ratio x ~ 1.7 has been reported by Liu *et al.*[21] for zirconia nanoparticles prepared by precipitation methods.

In addition to the metal-oxygen ratio, information on the contamination of the nanoparticles by other elements appeared of interest. Contaminations by H and C may be due to
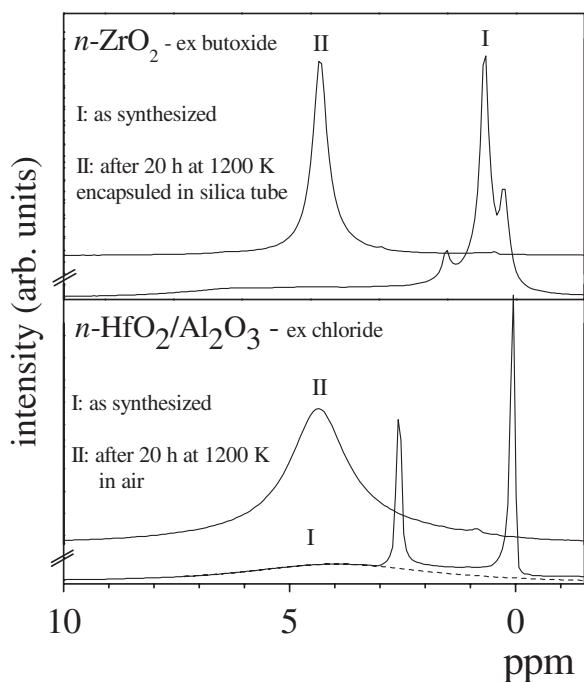
FIG. 1. ^{1}H MAS NMR spectra of nanocrystalline oxides (I) in the as-synthesized state and (II) after heating to 1200 K for 20 h.

the precursors used in the synthesis. Furthermore, it is known that the surface of oxides such as ZrO_2 and HfO_2, when exposed to the atmosphere, becomes covered by a hydrate layer which consists of chemisorbed hydroxyl groups and physisorbed water molecules. Thermogravimetry was employed as a first step to test for the presence of precursor fragments and hydrate layers. Noncoated zirconia nanoparticles synthesized from butoxide and chloride precursors, respectively, were found to lose as much as 10 and 5 wt %, respectively, when heated to 700 K. In commercial coarse-grained zirconia, the loss was less than 0.5 wt %.

For quantitative information on the elements involved in these large weight losses, we employed the ^{1}H MAS NMR technique and combustion elemental analysis.

^{1}H MAS NMR measurements were used to determine the hydrogen content of some of the samples investigated by PAC in the as-synthesized state and after high-temperature treatment. They were carried out with a Varian Infinity +spectrometer equipped with a 2.5 mm MAS-NMR double-resonance probe. The magnetic field strength was 9.4 T, corresponding to a ^{1}H resonance frequency of 401.52 MHz. The ^{1}H MAS-NMR spectra were acquired at 18 kHz spinning frequency using the saturation pulse sequence to reduce the probe and rotor background signals.[22] The spectra shown in Fig. 1 have been acquired at room temperature in typically 3 min with a repetition delay of 5 s, which is sufficient to obtain relaxed spectra. The ^{1}H chemical shifts refer to tetramethylsilane.

For the quantitative determination of the H contents, the integral of the NMR lines of precisely weighted quantities of the nano-oxides was compared to that of pure adamantan ($C_{10}H_{16}$; Aldrich) taken under identical experimental conditions.

The ^{1}H MAS NMR spectra of the nanoparticles in the as-synthesized state (for examples, see Fig. 1) typically showed several lines in the 0–10 ppm range, similar to the spectra observed by Chadwick *et al.*[23] for sol-gel produced nanocrystalline zirconia. The sharp lines at 0–3 ppm which disappear upon heating to 1200 K are probably caused by organic fragments. The broad resonance at ~4.9 ppm can be assigned to OH groups.[23] For the native particles, the H content was in the range of 5–10 wt %. The value reported by Chadwick *et al.*[23] for sol-gel produced n-ZrO_2 is of the same order of magnitude. Heating experiments showed that surprisingly high temperatures are required to completely expel the hydrogen from the plasma-synthesized particles. Heating the nano-oxides—either in air or encapsulated in quartz tubes—to 1200 K for 24 h decreased the H content by only a factor of 2 to the range 2.5–5 wt %, which may be taken as indication that hydrogen is not only involved in a surface hydrate layer but also penetrates into the oxide lattice, possibly occupying interstitial sites.[24] Heating to 1500 K in air for periods of 60 h was necessary to reduce the H content to 0.15 wt %, close to the limit of detection. For commercial cg-ZrO_2, we found ~0.35 wt %; after heating in air to 1200 K, we found ~0.2 wt %.

The NMR measurements were complemented by C-H-N-S elemental analysis. Using a LECO 932 combustion system (1300 K, 3 min), H and C concentrations of 1–2 wt % and 1 wt %, respectively, were detected in the nanoparticles. Considering the NMR observation that long-time exposure to temperatures $T \sim 1500$ K is required for complete H depletion of the nanoparticles, it is not surprising that the elemental analysis for 3 min at 1300 K results in a smaller value of the H content.

III. NANOPARTICLE STRUCTURE AND GRAIN GROWTH STUDIED BY TRANSMISSION ELECTRON MICROSCOPY AND X-RAY DIFFRACTION

A. Experimental details

For electron microscopic studies, a Philips (CM-30 ST or Tecnai F20 ST) transmission electron microscope was used to record electron diffraction spectra and high resolution images of the nanoparticles. The samples were prepared on copper grids covered with a holey carbon film by dipping a grid into the powder. Room temperature x-ray measurements (XRD) were carried out with a Philips (X'Pert) diffractometer, using Cu $K\alpha$ radiation. To study grain growth and structure changes with increasing temperature, selected powders were annealed at 473, 673, 873, and 1073 K for 6 h and at 1273 K for 20 h, respectively, in ambient air. For an estimate of the grain growth rate, some powder samples of noncoated n-HfO_2 were annealed at 1473 K for 15 min only. The particle size was determined from the linewidth of the XRD spectra (corrected for the instrumental resolution) by means of the Scherrer formula.[25] Commercial coarse-grained ZrO_2 was studied as purchased and after heating in air to 1673 K.

B. Structure of native HfO_2 and ZrO_2 nanoparticles

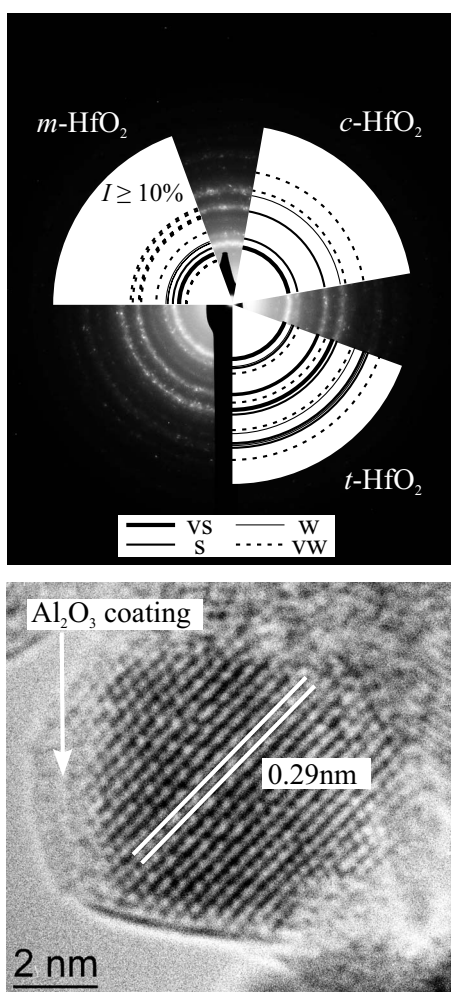The TEM micrographs of all nanoparticles—n-HfO_2, n-ZrO_2, bare or coated—provide clear evidence for a well-

FIG. 2. Electron diffraction pattern and TEM image of Al_2O_3-coated HfO_2 nanoparticles in the as-synthesized state. In the TEM image, the separation of lattice fringes is given. For comparison, the reference electron diffraction patterns of the monoclinic (Ref. 26), tetragonal (Ref. 26), and cubic (Ref. 27) phases of HfO_2 with their intensities are included. In the case of the monoclinic phase, only d values with intensity $I \geq 10\%$ are shown for the sake of clarity.

ordered, periodic structure of the Hf or the Zr sublattice in the native state. An example is given in Fig. 2, which shows the TEM image and electron diffraction pattern of Al_2O_3-coated HfO_2 nanoparticles. The HfO_2 core, surrounded by amorphous Al_2O_3, produces clearly visible lattice fringes. The fringe separations of 0.29 and 0.33 nm in coated and bare n-HfO_2, respectively, are consistent with the electron (Fig. 2) and x-ray diffraction patterns (Fig. 3). The comparison of the experimental and reference[26,27] electron diffraction patterns of HfO_2 shows that the coated particles crystallize mainly in the cubic or tetragonal phase, and the bare particles in the monoclinic phase. As a consequence of the very small particle size, the diffraction peaks of the as-synthesized state are strongly broadened and a distinction between the cubic and the tetragonal phase is, therefore, not possible.

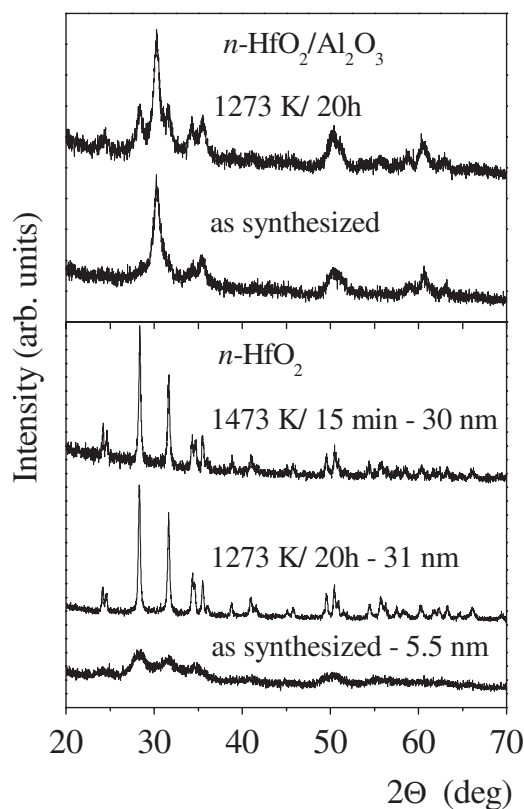In agreement with the TEM observations, the XRD spectrum of noncoated n-HfO_2 in the as-prepared state is dominated by the broadened lines of the monoclinic phase; that of coated n-HfO_2/Al_2O_3 shows the broadened reflections of the tetragonal or cubic phase (see Fig. 3). From the linewidths, one estimates a grain diameter of $d \sim 5.5$ and 10 nm for bare n-HfO_2 and n-HfO_2/Al_2O_3, respectively.

In contrast to nanocrystalline n-HfO_2 where bare particles crystallize in the monoclinic phase, the XRD spectra of both bare and coated n-ZrO_2 nanoparticles show the strongly broadened lines of tetragonal and/or cubic phases. Again, line broadening makes a distinction between cubic and tetragonal structures impossible. EXAFS measurements described in Ref. 28 favor the cubic structure. Reflections belonging to the monoclinic phase have not been found in the diffraction pattern of any of the native ZrO_2 nanoparticles. These observations agree with most reports on the room temperature structure of zirconia nanoparticles. One of the parameters which tend to stabilize the tetragonal over the monoclinic form is the contribution of the surface energy which increases with the surface area of the particles.[29] Other mechanisms of the room temperature stabilization of the metastable tetragonal phase of zirconia presently under discussion have recently been reviewed by Shukla and Seal.[30]

Similar differences between hafnia and zirconia regarding the phases occurring in the as-synthesized state were observed by Ushakov *et al.*[31] in a study of the crystallization of amorphous HfO_2 and ZrO_2 prepared by precipitation. According to these authors, the critical particle size for the tetragonal-to-monoclinic $(t \rightarrow m)$ transition of HfO_2 $(d_{cr}$

FIG. 3. Room temperature XRD spectra of n-HfO_2 and n-HfO_2/Al_2O_3 as synthesized and after annealing in air for 20 h at 1273 K. Additionally, the effect of rapid high-temperature annealing (15 min at 1473 K) on n-HfO_2 is illustrated.
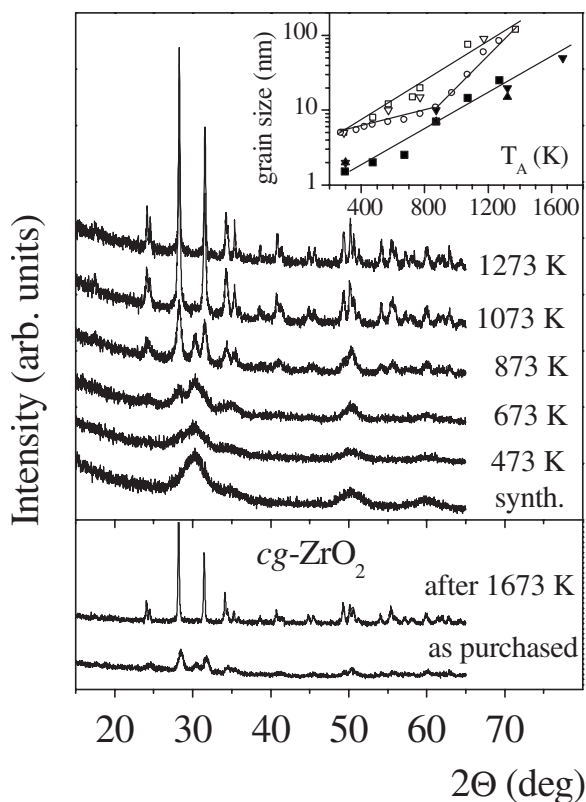
FIG. 4. XRD spectra of n-ZrO$_2$ at room temperature after annealing the sample for 6 h at the temperatures given. The inset illustrates the particle growth with temperature for samples synthesized by microwave plasma (full symbols; this work), by gas phase condensation (open circles; Ref. 40), and by hydrothermal methods (open squares and triangles; Refs. 37 and 38). The bottommost section shows the room temperature XRD spectra of coarse-grained ZrO$_2$ as purchased and after annealing at 1673 K for 6 h.

$\sim$6 nm) is considerably smaller than that of ZrO$_2$ (d_{cr} $\sim$20 nm, see below). As a consequence, amorphous HfO$_2$ favors the transformation into the monoclinic phase, while amorphous ZrO$_2$ always transforms into the tetragonal phase. Only amorphous HfO$_2$ with very high surface area is reported to transform to the tetragonal phase (particle diameter $d \lesssim 3$ nm $< d_{cr}$). Our measurements suggest a critical particle size of $d_{cr} \lesssim 5.5$ nm for the $t \rightarrow m$ transformation of n-HfO$_2$.

In summary, both TEM images and XRD spectra provide evidence for a periodic cation sublattice of all native nanoparticles. Bare and coated ZrO$_2$ nanoparticles crystallize in the tetragonal or cubic modification. In nanocrystalline HfO$_2$, however, this high-temperature modification is observed only when the nanoparticles are coated with Al$_2$O$_3$. We found no evidence that the structure of the native state is affected by the precursor used in the synthesis.

C. Grain growth of nanocrystalline ZrO$_2$ and HfO$_2$

Temperature-induced particle growth was studied by taking the room temperature XRD spectra of ZrO$_2$ and HfO$_2$ nanoparticles annealed at increasing temperatures. Figure 4 shows a series of XRD spectra of bare ZrO$_2$ nanoparticles.

As the annealing temperature is increased, the width of the x-ray reflections becomes narrower and the diffraction pattern of monoclinic ZrO$_2$ starts to emerge. Up to annealing temperatures $T_A < 1000$ K, one finds a mixture of m- and t/c-ZrO$_2$; after $T_A \geq 1073$ K, all particles are in the monoclinic phase. The inset of Fig. 4 shows the grain diameter d of bare n-ZrO$_2$, deduced from the XRD linewidth using the Scherrer formula,[25] as a function of the annealing temperature T_A. From these data, one obtains a critical particle size for the $t \rightarrow m$ transformation of $d_{cr} \sim 20$ nm, in good agreement with the value reported by Petrunin et al.[32] (d_{cr} $\sim$20 nm) for n-ZrO$_2$ prepared by heat treatment of amorphous ZrO(OH)$_2$ hydroxide, and the result of Chraska et al.[33] ($d_{cr} \sim 18$ nm) for zirconia nanoparticles produced by plasma spraying of an organometallic precursor. For amorphous ZrO$_2$ prepared by precipitation, Ushakov et al.[31] have obtained $d_{cr} \sim 30$ nm. Guo and Chen[34] have recently reported the synthesis of monoclinic zirconia particles with a particle diameter as small as $d \sim 15$ nm.

The variation of the particle size with annealing temperature (inset in Fig. 4) is well described by the relation ($d - d_0) \sim \exp(-Q_A/k_B T_A)$ expected for grain growth in an isochronous annealing experiment.[35] The grain growth activation enthalpy is $Q_A = 32(5)$ kJ/mole for both the monoclinic and the tetragonal or cubic phase, which agrees well with the value obtained by Xiong et al.[36] and Siu et al.[37] for nanoscaled zirconia prepared by the hydrothermal method [$Q_A = 26(6)$ kJ/mol; open symbols in Fig. 3]. Kirsch et al.[38] have found $Q_A = 33(8)$ kJ/mol for n-ZrO$_2$ colloids. In a neutron diffraction study of n-ZrO$_2$ produced by freeze-drying, Baldinozzi et al.[39] arrived at $Q_A \approx 40$ kJ/mol. The data of Würschum et al.[40] (open circles in Fig. 4) for n-ZrO$_2$ prepared by gas phase condensation (formation of Zr nanoparticles, subsequent oxidation, and in situ compaction) correspond to $Q_A = 61(5)$ kJ/mol for $T_A > 700$ K. The XRD patterns in the bottommost section of Fig. 4 illustrate that a high-temperature treatment is required to obtain a well crystallized sample of commercial cg-ZrO$_2$.

Alumina-coated n-ZrO$_2$/Al$_2$O$_3$ and n-HfO$_2$/Al$_2$O$_3$ are similar in their annealing behavior. After heating to $T_A = 1273$ K, both coated species show a mixture of the monoclinic ($d \sim 16$ nm) and the tetragonal or cubic ($d \sim 10$ nm) phase. At the same annealing conditions, noncoated particles have reached a larger size, which is consistent with the observation of Kirsch et al.[38] that alumina coating of zirconia colloids inhibits the zirconia cores from coarsening. The retention of the tetragonal phase in coated particles up to high temperatures can be attributed to the volume expansion of $\sim$4.5% at the monoclinic-tetragonal transformation. In particles mechanically confined by an Al$_2$O$_3$ coating, this expansion leads to compressive stresses which stabilize the tetragonal phase.

Grain growth of bare monoclinic n-HfO$_2$ was found to be surprisingly fast. At $T_A = 1473$ K, an annealing time $t_A \leq 15$ min was sufficient to reach a particle diameter of $d \sim 30$–35 nm, both for powder samples and pellets compacted with a pressure of 0.4 GPa (see lower section of Fig. 3 and the 1400 K/15 min PAC spectrum in Fig. 6). Extrapolating the n-ZrO$_2$ neutron diffraction results of Baldinozzi et

al.[39] ($t_A \sim 200$ min to grow from $d_0 = 13.7$ nm to $d \sim 35$ nm at $T_A = 923$ K) to $T_A = 1473$ K, using $Q_A \sim 40$ kJ/mol, one would expect that at 1473 K, it will take $t_A \geqslant 50$ min to get to $d \sim 30$–35 nm. Apparently, n-HfO$_2$ studied here and n-ZrO$_2$ of Ref. 39 differ considerably in the parameters that control the grain growth (activation enthalpy and initial surface free energy).

IV. ^{181}Hf/^{181}Ta PERTURBED ANGULAR CORRELATION MEASUREMENTS

A. Experimental details

In most of the PAC measurements reported here, the isotope ^{181}Ta was used as probe nucleus. The excited states of ^{181}Ta are populated in the β^- decay of ^{181}Hf ($T_{1/2} = 45d$). ^{181}Hf is easily produced by thermal neutron capture: ^{180}Hf (n, γ) ^{181}Hf. For the production of the PAC sources, a few milligrams of nanoparticles of HfO$_2$ and ZrO$_2$ (doped with a Hf concentration of ~ 4 at. %) were enclosed under vacuum into fused silica tubes and irradiated in a flux of thermal neutrons of 5×10^{13} n/s cm^2 for times of the order of 1 and 24 h, respectively. The PAC measurements on ZrO$_2$ nanoparticles were carried out with powder samples. The question of whether differences in the heat transfer affect the QI parameters and the phase transformations was addressed with hafnia nanoparticles by studying both powder samples and pellets compacted with a pressure of 0.4 GPa prior to the neutron activation.

Sources of coarse-grained HfO$_2$ and ZrO$_2$ (noncompacted) were produced by irradiating commercially available compounds. Unless special care is taken, commercial ZrO$_2$ contains a Hf concentration of 1–2 at. %.

To study the possible influence of the H concentration detected by the ^{1}H-MAS NMR technique on the hyperfine interaction seen by the probe nuclei, two samples of n-HfO$_2$—one coated, the other noncoated—were outgassed by heating to 1500 K for 60 h. A H content of 0.15 wt % was established by ^{1}H-MAS NMR analysis prior to encapsulation and neutron irradiation.

The silica tubes were mounted in a furnace designed for high-temperature PAC measurements (see Ref. 41). The PAC spectra of the 133–482 keV cascade of ^{181}Ta were measured as a function of temperature in the range 290 K$\leqslant T$ $\leqslant 1550$ K. Two temperature programs were carried out. In the "continuous heating and cooling" program, the sample temperature was monotonously raised in steps of 50–100 K and, after reaching the maximum value, lowered in similar steps back to room temperature. In the "cycling" program, a room temperature measurement was carried out after each temperature increase between 300 and 1550 K. The spectra were taken with a standard four-detector setup equipped with fast BaF$_2$ scintillators. Their truncated conical shape allows a minimum sample-detector distance of 11 mm.

B. Data analysis

For polycrystalline samples, the time modulation of the angular correlation coefficients A_{kk} ($k = 2, 4$) of a cascade of two successive γ rays by a hyperfine interaction can be ex-

pressed by a perturbation factor $G_{kk}(t)$ which, in the most general case, depends on the multipole order, the symmetry and time dependence of the interaction, and the spin of the intermediate state of the cascade. In the present case of a static electric QI and nuclear spin $I = 5/2$, the perturbation function $G_{kk}(t; \nu_q, \eta, \delta)$ is a well-known function of the quadrupole frequency $\nu_q = eQV_{zz}/h$, the asymmetry parameter $\eta = (V_{xx} - V_{yy})/V_{zz}$, and a relative linewidth δ describing an eventual distribution of the static QI caused by structural, chemical, and other defects (for details, see, e.g., Refs. 42 and 43). In the present study, a Lorentzian QI distribution (δ=full with at half maximum) was used in the analysis. $V_{ii} = d^2V/di^2$ ($i = x, y, z$) are the principal-axis components of the EFG tensor with $|V_{xx}| \leqslant |V_{yy}| \leqslant |V_{zz}|$.

When several fractions of nuclei subject to different QIs are found in the same sample, the effective perturbation factor is given by

$$G_{kk}(t) = \sum_i f_i G_{22}^i(t; \nu_q^i, \eta^i, \delta^i), \qquad (1)$$

where f_i (with $\Sigma_i f_i = 1$) is the relative intensity of the ith component.

For γ-γ cascades with vanishing angular correlation coefficient A_{44}, the perturbation factor $G_{22}(t)$ can be determined by taking coincidence spectra $N(\Theta, t)$ at the angles $\Theta = 90°$ and 180° between two detectors:

$$A_{22}^{\text{expt}} \sum_i f_i G_{22}^i(t) = 2[N(180, t) - N(90, t)]/[N(180, t)$$
$$+ 2N(90, t)]. \qquad (2)$$

In the experiment, the anisotropy coefficient A_{22} of the γ-γ cascade is modified by the experimental conditions, such as the finite solid angle extended by the detectors, the time resolution relative to the precession period, eventual prompt coincidences, and other factors. As described in detail in Ref. 44, the experimental anisotropy A_{22}^{expt} of our setup has been determined by measuring the ^{181}Ta PAC of a source of HfOCl$_2$ dissolved in dilute HCl as a function of the source-detector distance. [Note: The finite solid angle integration attenuates the coefficient A_{44} stronger than the coefficient A_{22}. The 133–482 keV cascade of ^{181}Ta has a coefficient $A_{44} \sim 0.07$. The large solid angle of our setup, however, leads to $A_{44}^{\text{expt}} \approx 0.0$ which justifies the neglect of the A_{44} term in Eq. (2)].

For the extraction of the relative intensities f_i and the QI parameters $\{\nu_q^i, \eta^i, \delta^i\}$ of the different components i in the PAC spectra of the hafnia and zirconia nanoparticles, the expression $A_{22}^{\text{expt}} \Sigma_i f_i G_{22}^i(t; \nu_q^i, \eta^i, \delta^i)$ was fitted to the measured spectra, with the value of A_{22}^{expt} for the given sample-detector distance as fixed parameter.

C. Results

1. ^{181}Ta *perturbed angular correlation of coarse-grained* HfO$_2$ *and* ZrO$_2$

For clear identification of possible particle size effects, we first established a basis of comparison by a detailed study of
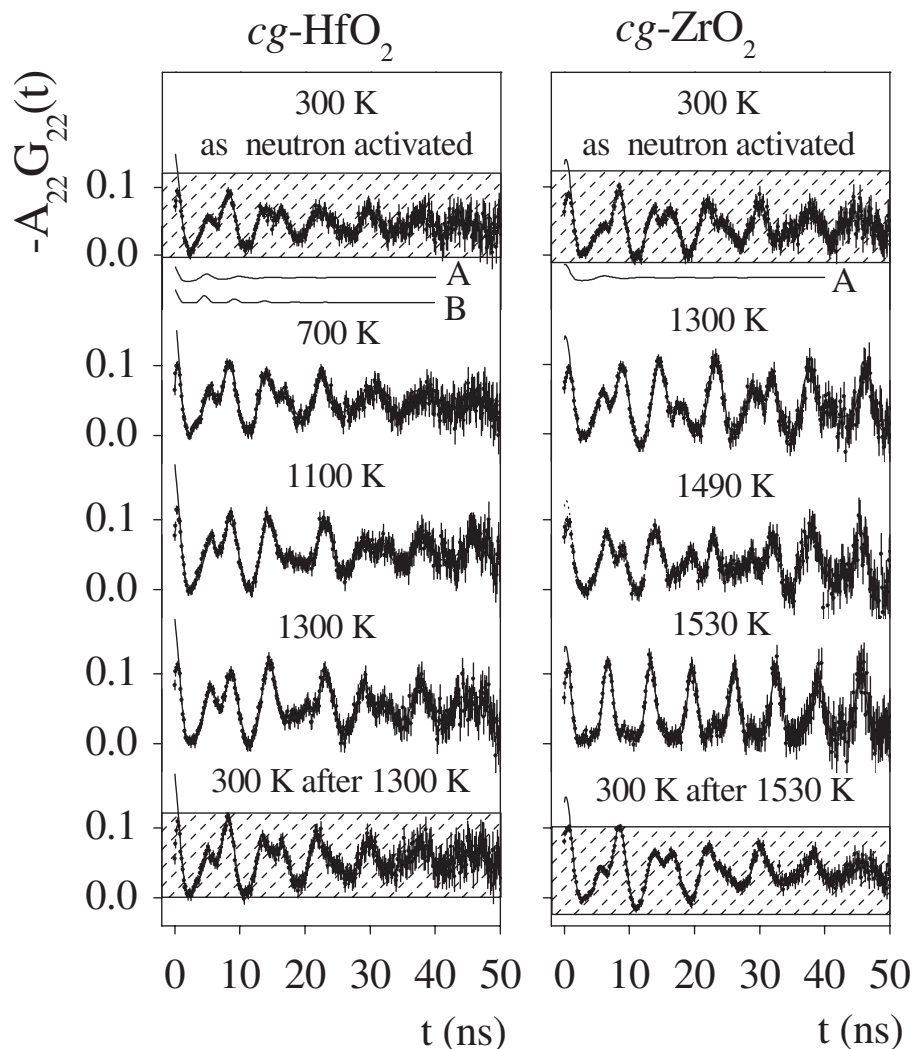
FIG. 5. PAC spectra of ^{181}Ta in powder samples (in vacuum) of coarse-grained HfO$_2$ (left-hand column) and ZrO$_2$ (right-hand column) at different temperatures. The solid lines below the topmost spectra represent the perturbation factor of the disordered component; curves A for a static QI distribution; curve B for a slowly fluctuating QI. The height of the striped areas is a measure of the monoclinic fraction at 300 K after the samples passed through 1300 and 1530 K, respectively.

commercial coarse-grained (cg-) oxides. Figure 5 shows typical PAC spectra of ^{181}Ta in cg-HfO$_2$ (left-hand column) and cg-ZrO$_2$ (right-hand column) at different temperatures. In the case of cg-HfO$_2$, the sample was cycled between increasing values of T and 300 K, while cg-ZrO$_2$ was subject to a continuous heating and cooling program with a maximum temperature of 1550 K. The PAC spectra of ^{181}Ta in cg-HfO$_2$ show the well-known nonperiodic oscillation pattern of monoclinic (m-) HfO$_2$ at all temperatures 300 K $\leq T$ $\leq$ 1500 K. Cooling below room temperature leaves the pattern unchanged (ν_q=811 MHz; η=0.336 at 15 K; Ref. 45). In the case of cg-ZrO$_2$, the analog pattern of m-ZrO$_2$ transforms to the periodic oscillation of tetragonal (t-) ZrO$_2$ at $T>1400$ K. The slight differences in the experimental anisotropy close to the time zero point between HfO$_2$ and ZrO$_2$ are due to prompt coincidences from the decay of radioactive ^{95}Zr produced by neutron irradiation.

Two components are required for a description of the room temperature spectra of both compounds in the as-purchased state. The dominant components with the well-known QI parameters of m-HfO$_2$ (Ref. 11) and m-ZrO$_2$ (Ref. 12) have relative intensities of $f_1\sim75\%$ and 80%, respectively. The QI parameters of ^{181}Ta in the monoclinic phases at 300 K are listed in Table I. Their temperature dependence

TABLE I. The QI parameters (ν_q, η, and δ) and the relative intensities of the two components present in the PAC spectra of ^{181}Ta in coarse-grained HfO$_2$ and ZrO$_2$ at 300 K.

Component	Relative intensity	ν_q (MHz)	η	δ
		cg-HfO$_2$		
I-monoclinic	0.75	793(2)	0.345(5)	0.07(1)
II-QI distribution (A)	0.25	1300(100)	0.3–0.4	0.4(10)
		cg-ZrO$_2$		
I-monoclinic	0.8	802(2)	0.335(5)	0.025(1)
II-QI distribution (A)	0.2	1200(100)	0.3–0.4	0.4(1)

agrees with that reported in Refs. 11 and 12. The minority component II mainly shows up in the fact that the value of the anisotropy needed to describe the spectra at delay times $t > 5$ ns is substantially smaller than the experimentally determined A_{22}^{expt}. This implies that the perturbation factor of this fraction decreases rapidly within the first few nanoseconds. At larger delay times, the PAC pattern contains no other oscillatory components than those of the monoclinic oxide. The interaction of component II is, therefore, difficult to identify. In principle, there are two possibilities: The fast initial decrease might reflect either a static distribution of strong QIs or be caused by a fluctuating interaction. In the case of a slow fluctuation of the QI, the perturbation factor can be approximated[46,47] by $G_{kk}(t) = \Gamma_{kk}(t)\, e^{-\lambda_k t}$, with $\Gamma_{kk}(t)$ describing the static perturbation and λ_k the nuclear spin relaxation. The full lines below the topmost 300 K spectra of cg-HfO$_2$ and cg-ZrO$_2$ in Fig. 5 (slightly shifted toward smaller anisotropy for the sake of clarity) illustrate the perturbation factor of the component II for the case of a static QI distribution (A) and a dynamic perturbation (B) with a relaxation parameter of the order of $\lambda_2 \sim 300\text{–}400$ MHz. Clearly, the two possibilities are hard to distinguish.

2. ^{181}Ta *perturbed angular correlation of nanocrystalline* HfO$_2$ *and* ZrO$_2$

Overview. The nanocrystalline oxides investigated here can be divided into four groups: noncoated n-HfO$_2$ and n-ZrO$_2$, and coated n-HfO$_2$/Al$_2$O$_3$ and n-ZrO$_2$/Al$_2$O$_3$, respectively. At least two powder samples of each oxide were studied, one subject to continuous heating and cooling, the other cycled between temperature T and 300 K, respectively. In the case of n-HfO$_2$ and n-HfO$_2$/Al$_2$O, we also investigated pellets compacted with a pressure of 0.4 GPa. Characteristic ^{181}Ta PAC spectra of bare n-HfO$_2$ and n-ZrO$_2$ are shown in Fig. 6. Figure 7 correlates PAC and XRD spectra of n-HfO$_2$/Al$_2$O$_3$ at different temperatures. For typical spectra of coated n-ZrO$_2$/Al$_2$O$_3$, see Forker *et al.*[6]

In all nano-oxides—bare and coated, powder samples and pellets—the first room temperature spectra after neutron irradiation (topmost in Figs. 6 and 7) are characterized by strongly damped oscillatory structures, in many cases even by the total absence of any oscillations, which is an indication of a broad distribution of strong QIs. The parameters of this QI distribution are $\nu_q \sim 1100\text{–}1200$ MHz, $\eta \sim 0.2\text{–}0.4$, and $\delta \sim 0.4\text{–}0.6$ both for hafnia and zirconia nanoparticles.

In the following, we shall concentrate on the results for the coated and noncoated HfO$_2$ nanoparticles. In the case of the nanocrystalline zirconia, we report those results which go beyond the data obtained in our earlier study,[6] i.e., the behavior observed upon cooling from $T \leqslant 1500$ K.

Nanocrystalline HfO$_2$ *at* $T > 300$ K. Upon heating of bare and coated n-HfO$_2$ particles, the nonperiodic oscillation pattern of monoclinic HfO$_2$ starts to emerge at the expense of the broad QI distribution (see Figs. 6 and 7), and the PAC pattern of cg-HfO$_2$ is reached at $T \sim 1200$ and 1400 K, respectively. At high temperatures, the well-ordered monoclinic phase develops rapidly: When native n-HfO$_2$ and n-HfO$_2$/Al$_2$O$_3$ are heated—within 2–3 min—from 300 to 1400 K, the monoclinic phase reaches an intensity of

$\sim$80% within the first 15 min (see the 1400 K spectrum in the center of the left-hand column of Fig. 6), which is consistent with the XRD spectrum of n-HfO$_2$ annealed for 15 min at 1473 K shown in Fig. 3.

All spectra of the first heating sequence after neutron activation (300 K $\leqslant T \leqslant$ 1450 K) could be well described by a two-fraction model, one component with the QI parameters of monoclinic HfO$_2$, the other one with the parameters of the broad frequency distribution observed in the "as-synthesized" state. In none of the hafnia samples investigated did we find an indication of tetragonal HfO$_2$ which would show up as a component with a periodic ($\eta = 0$) oscillation pattern (as an example, see the periodic pattern of t-ZrO$_2$ at 1530 and 1400 K in Figs. 5 and 6, respectively). Figures 8 and 9 show the relative intensity f_m and the relative linewidth δ_m of the monoclinic phase in coated and noncoated hafnia nanoparticles as a function of temperature. Figure 8 illustrates the typical behavior observed in a continuous heating and cooling program, Fig. 9 the behavior found in a cycling experiment. In all cases, the monoclinic fraction at T increases with temperature to reach saturation $f_m \geqslant 0.95$ at $T \geqslant 1200$ and 1400 K for n-HfO$_2$ and n-HfO$_2$/Al$_2$O$_3$, respectively. The increase of the monoclinic fraction f_m is accompanied by an irreversible decrease of the QI linewidth δ_m. As illustrated by Fig. 7, the degree of order characterized by the QI linewidth δ_m and the grain size d are correlated: The sharper the XRD lines, the less the damping of the oscillation amplitudes of the PAC spectra. The correlation $\delta \propto 1/d$ has also been observed in the ^{181}Ta PAC spectra of nanocrystalline TiO$_2$.[44]

The most remarkable aspect of the data in Figs. 8 and 9 is the pronounced decrease of the monoclinic fraction f_m upon cooling. When continuously lowering the temperature (open symbols in Figs. 8 and 9, left-hand column) from $T \sim 1500$ K, f_m remains constant down to $T \sim 700$ K, and then drops by about 35% within a temperature interval of $\sim$150–200 K. The frequency distribution of the remaining monoclinic component, however, maintains the narrow linewidth δ_m (open symbols in Figs. 8 and 9, right-hand column) reached at $T \sim 1500$ K.

The reduction of the monoclinic intensity f_m observed for the nanoparticles indicates that below $T \sim 700$ K, a large fraction of the probe nuclei in these particles becomes subject to a different QI. As in the native coarse-grained oxides, this second component (in the following termed "defect" component) mainly shows up as a pronounced loss of anisotropy in the first few nanoseconds. Again, at larger delay times, the PAC pattern contains no other oscillatory components than those of the monoclinic oxide. The solid lines below the 300 K spectra in Fig. 6 show the perturbation factor of the defect component needed to reproduce the experimental spectra at $T < 700$ K; curves A are obtained for a static QI distribution, curves B for a fluctuating QI.

It is important to stress that the appearance of this defect component, which has been found for all nanoparticles—bare, coated, and outgassed, in powder samples and pellets and for all precursors—is fully reversible: Upon cooling from $T > 1200$ K, the monoclinic fraction drops to $f_m \sim 0.65$ at $T \leqslant 500$ K, but by heating to $T > 800$ K, its saturation value $f_m \geqslant 0.95$ is promptly restored.
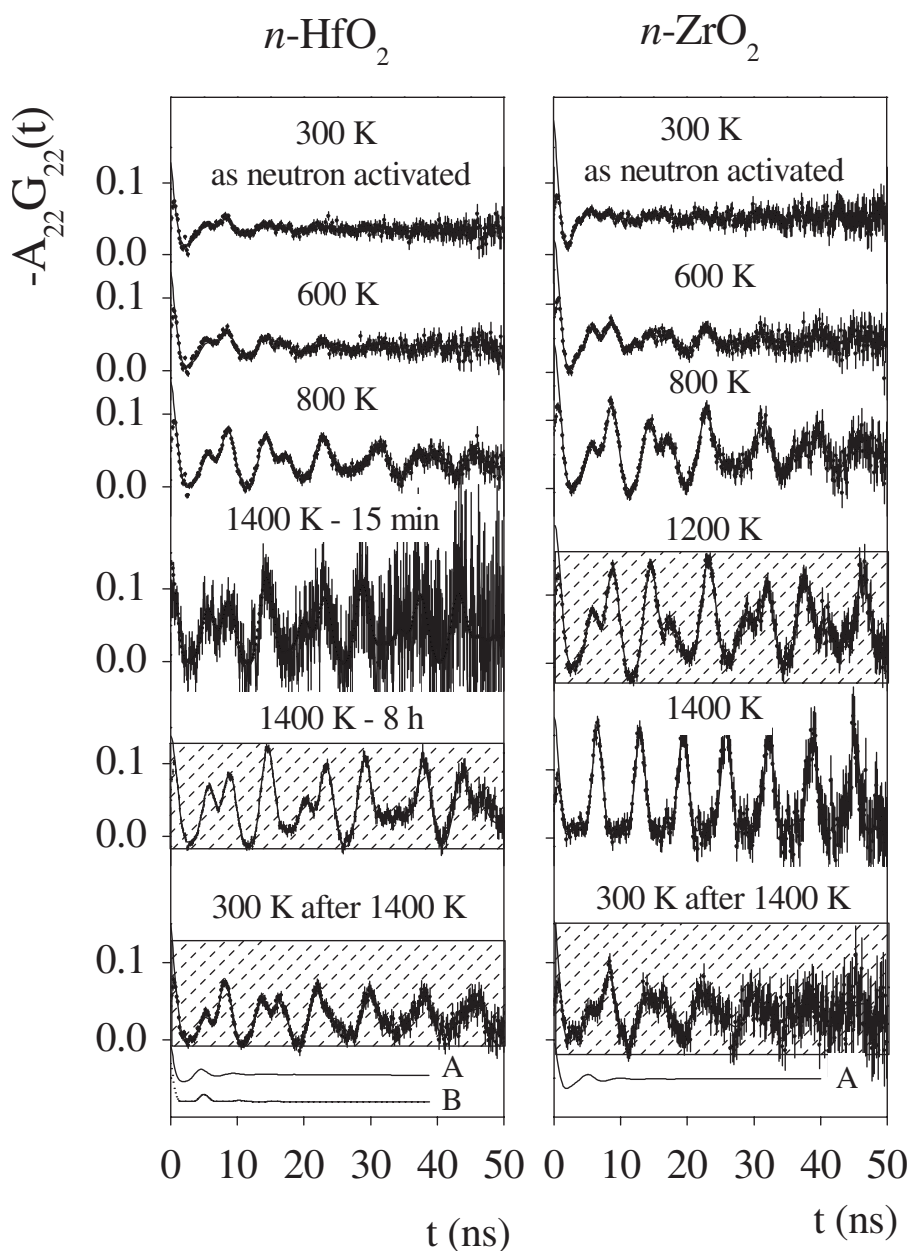
FIG. 6. PAC spectra of ^{181}Ta in powder samples (in vacuum) of bare HfO$_2$ (left-hand column) and ZrO$_2$ nanoparticles (right-hand column) at different temperatures. For n-HfO$_2$, two spectra taken at 1400 K are shown. The upper one has been accumulated within the first 15 min after a virgin sample of n-HfO$_2$ had been heated (within 2–3 min) from 300 to 1400 K. The lower one shows the spectrum accumulated at 1400 K in the subsequent 8 h. The height of the striped areas is a measure of the monoclinic fraction of n-HfO$_2$ and n-ZrO$_2$ at $T=1400$ and 1200 K, respectively.

The reversible appearance of a defect component at the expense of the monoclinic fraction upon cooling was also observed when the nanoparticles were cycled between an elevated temperature T and 300 K. The effect is easily seen in Fig. 9, where from $T \sim 700$ K onwards, $f_m(300 \text{ K})$ is significantly smaller than $f_m(T)$, while $\delta_m(300 \text{ K}) \sim \delta_m(T)$. Cooling from 1300 to 300 K results in a pronounced loss of amplitude; the attenuation of the oscillations with time, however, is not affected. The difference $[f_m(1400 \text{ K}) - f_m(300 \text{ K})]$ was found to be independent of the time (within 100 h) the sample was kept at 1400 K.

Due to the lack of oscillatory structure of the defect component, the precision of its QI parameters is as limited as that of component II of the cg-oxides. Assuming a static QI distribution, one obtains QI parameters of the order $\nu_q \sim 1100$–1300 MHz, $\eta \sim 0.3$–0.5, and $\delta \sim 0.4$–0.6, which are quite similar to those of component II of the coarse-grained oxides (cf. Table I).

The two samples from which the hydrogen had been expelled—at least to a large extent—prior to neutron activation also presented the reduction of f_m. In addition to the defect component encountered in all other oxides, a second
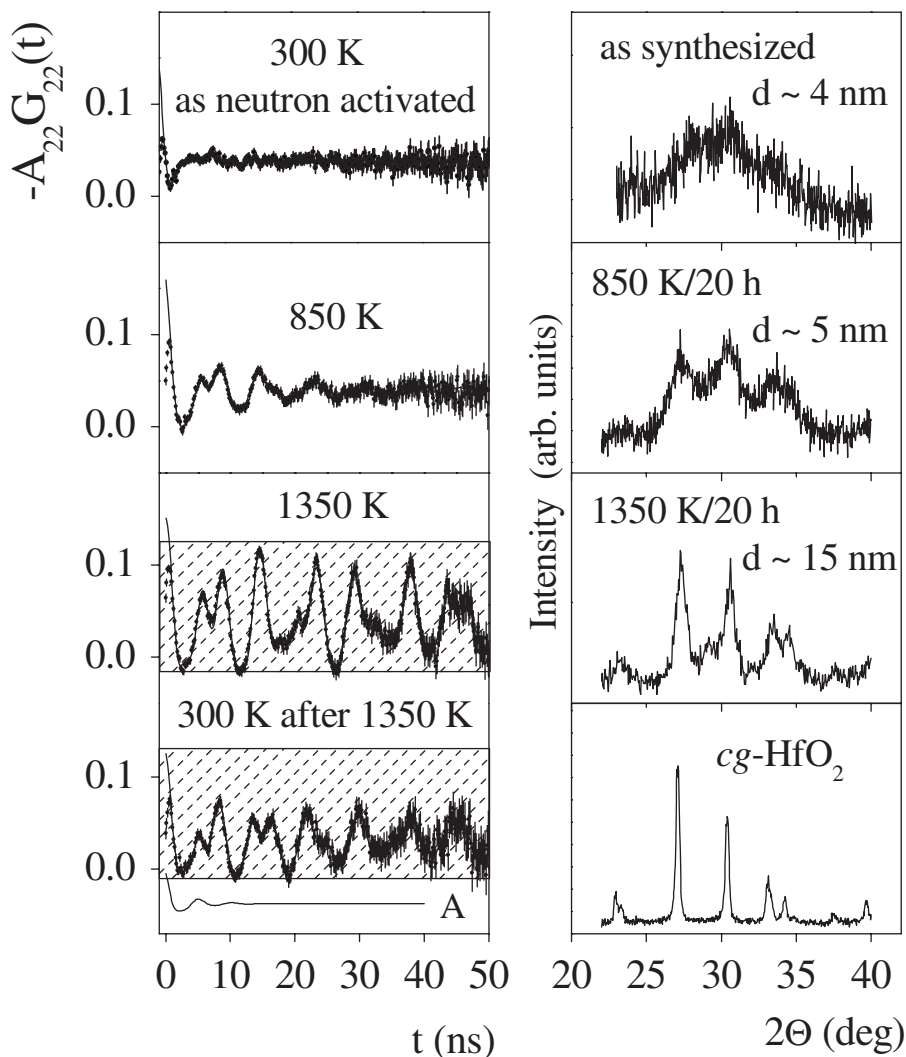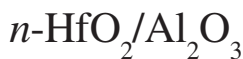
FIG. 7. PAC spectra of ^{181}Ta in Al$_2$O$_3$-coated nanoparticles of HfO$_2$ (powder sample in vacuum) at different temperatures (left-hand column), and room temperature x-ray diffraction spectra of n-HfO$_2$/Al$_2$O$_3$ after synthesis and after annealing at 850 and 1350 K, respectively (right-hand column). The height of the striped area is a measure of the monoclinic fraction at 1350 K. The particle size has been derived from the linewidth of the x-ray reflections. For comparison, the x-ray pattern of commercial cg-HfO$_2$ is shown in the bottommost section of the right-hand column.

component was observed upon cooling. This new component (intensity $f \sim 0.2$ and relative linewidth $\delta \sim 0.25$) showed an extremely short spin precession period of ~ 3 ns, corresponding to $\nu_q \sim 2400$ MHz for $\eta = 0$ or $\nu_q \sim 1200$ MHz for $\eta = 1$.

Nanocrystalline ZrO$_2$ *at* $T > 300$ K. While in nanoscaled hafnia only the monoclinic phase appears upon heating, both the monoclinic and the tetragonal phase are present in all nanoscaled zirconia. With increasing temperature, the PAC spectrum passes from a broad QI distribution through the nonperiodic pattern of m-ZrO$_2$ and the periodic pattern of t-ZrO$_2$, and upon cooling, m-ZrO$_2$ reappears, in agreement with our previous results[5,6] for n-ZrO$_2$. The analysis of the spectra of the nanoscaled zirconia, therefore, requires a three-component model. Typical data for the temperature dependence of the relative intensities of the monoclinic and the

tetragonal phase in n-ZrO$_2$ and n-ZrO$_2$/Al$_2$O$_3$ are collected in Fig. 10 together with those of cg-ZrO$_2$.

When the zirconia nanoparticles are cooled from $T \sim 1550$ K, one first observes the transformation of the tetragonal phase into the monoclinic phase, which occurs gradually in the case of the coated n-ZrO$_2$/Al$_2$O$_3$ and rather sharply in the noncoated particles. Upon further cooling, the same change happens as in the hafnia nanoparticles: The relative intensity of the monoclinic fraction f_m suffers a reversible reduction (see Fig. 10), while the linewidth δ_m retains the small high-temperature value.

The reduction of f_m caused by the appearance of the defect component takes place in slightly different temperature ranges: at $700-500$ K in the hafnia, at $450-350$ K in the zirconia particles; the relative decrease of f_m, however, is of the same order of $35\%-40\%$ in both cases.
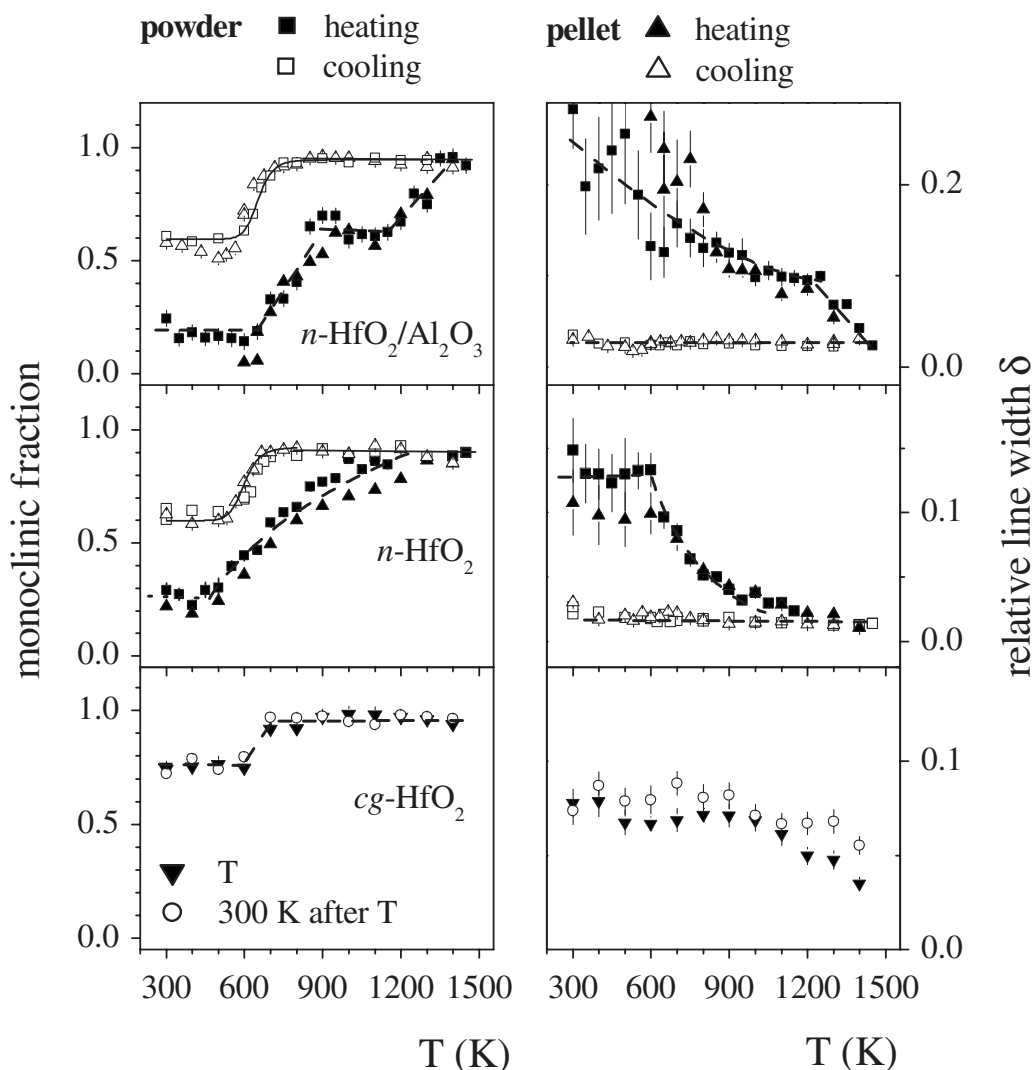
FIG. 8. The monoclinic fraction and the relative linewidth of the QI of ^{181}Ta in bare and coated nanoparticles of HfO$_2$ and coarse-grained HfO$_2$ (from top) as a function of temperature. Data for nano-oxide powders and pellets are shown. The nanoparticles were continuously heated to $T \le 1550$ K and cooled back to 300 K, whereas the coarse-grained oxide was cycled between temperature T and 300 K. For cg-HfO$_2$, the plot shows at a given T both the monoclinic fraction $f_m(T)$ measured at this temperature (solid downward triangles) and the fraction $f_m(300 \text{ K})$ (open circles) observed at 300 K after cooling from T. Note that $f_m(300 \text{ K}) = f_m(T)$ for all T. The solid lines at $T < 800$ K represent fits of Eqs. (3) and (4) to the monoclinic fraction of the nanoparticles measured when cooling from 1450 K.

The data of cg-HfO$_2$ and cg-ZrO$_2$ included in Figs. 8 and 10, respectively, illustrate that the bulk material presents a different behavior: Here, the monoclinic fraction maintains its high-temperature value upon cooling. [Note: cg-HfO$_2$ was cycled between T and 300 K, and the plot in the bottommost section of Fig. 8 shows at a given T both the monoclinic fraction $f_m(T)$ measured at this temperature and the fraction $f_m(300 \text{ K})$ observed at 300 K after cooling from T. One finds $f_m(300 \text{ K}) = f_m(T)$ at all T.]

Obviously, the appearance of the defect component in the ^{181}Ta PAC spectra is correlated to the particle size. The same particle size effect has been observed in the ^{181}Ta PAC study of n-ZrO$_2$ particles synthesized by gas phase condensation,[5] which grow faster with temperature than those produced by the microwave plasma (see inset of Fig. 4). In that PAC experiment,[5] the sample was annealed at increasing temperatures T_A and, after each annealing step, the ^{181}Ta PAC was

measured at room temperature. For grain sizes $d \le 50$ nm (determined by XRD), the monoclinic fraction $f_m(290 \text{ K})$ remained far below the saturation value: $f_m(290 \text{ K}) \le 0.6$. However, when d exceeded 100 nm at $T_A \ge 1400$ K, the monoclinic fraction saturated at $f_m(290 \text{ K}) \sim 1$, i.e., the defect component had disappeared.

At 1450 K, the grain size of the microwave-plasma particles studied in the present paper does not exceed $d \sim 30$ nm and, in these particles, about one-third of the probe nuclei are subject to the defect interaction upon cooling below $T \sim 700$ K. The comparison of the previous[5] and the present PAC experiments then suggests a critical grain diameter $d < 100$ nm for the appearance of the defect component.

A particle size effect has also been reported in an electron spin resonance study of ZrO$_2$ nanopowders by Liu *et al.*[21] These authors have detected a surface-related paramagnetic F-center signal which they attribute to the trapping of elec
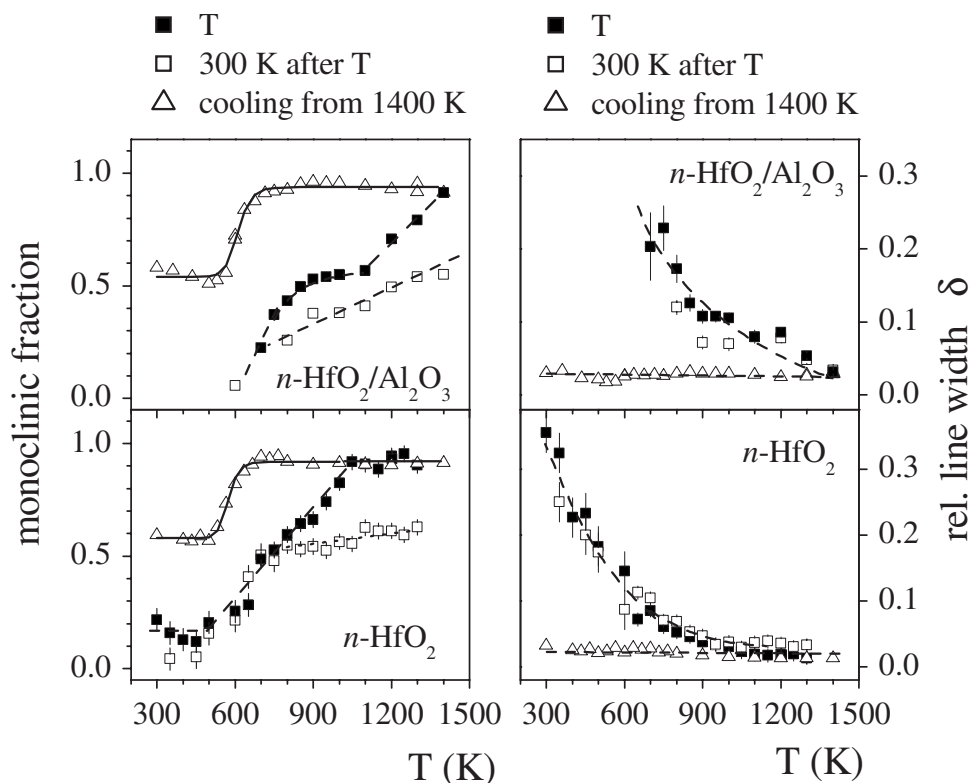
FIG. 9. The monoclinic fraction and the linewidth of the QI of ^{181}Ta in bare and coated nanoparticles of HfO$_2$ as a function of temperature. The powder samples (in vacuum) were cycled between T (full squares) and 300 K (open squares), and at the end, continuously cooled from 1400 K. The solid lines represent fits of Eqs. (3) and (4) to the monoclinic fraction measured upon cooling from 1400 K.

trons in grain-boundary oxygen vacancies. The intensity of the F-center signal decreases with increasing particle size and disappears at $d > 50$ nm.

Finally, we mention that the ^{181}Ta QI parameters ν_q and η of annealed ZrO$_2$ and HfO$_2$ nanoparticles, bare or coated, at different temperatures agree, within the experimental accuracy, with those of the coarse-grained materials.

V. ^{111}In/^{111}Cd PERTURBED ANGULAR CORRELATION MEASUREMENTS

For more information on the mechanism that leads to the appearance of the defect component in the ^{181}Ta PAC spectra of the nanocrystalline oxides at $T < 700$ K, it appeared of interest to broaden the investigation of QIs in nanocrystalline oxides to other probe nuclei.

Luthin *et al.*[48] have used the nucleus ^{111}In/^{111}Cd—another favorable PAC radioisotope—for a PAC study of electric quadrupole interactions in coarse-grained HfO$_2$ and ZrO$_2$. We have extended these ^{111}Cd QI studies to noncoated nanocrystalline HfO$_2$ and ZrO$_2$. The 171–245 keV γ-γ cascade of ^{111}Cd is populated by the electron capture decay of ^{111}In ($T_{1/2} = 2.8d$). Sample preparation, therefore, requires doping of the nanoparticles with radioactive ^{111}In. Oxides have been successfully doped with ^{111}In by adding the radioactivity to the solution from which the oxides were precipitated.[49,50] The microwave-plasma process used here excludes the possibility of radioactive doping dur-

ing synthesis. Attempts to introduce the probe nuclei after synthesis by diffusion at $T \sim 1500$ K—starting from ^{111}InCl$_3$—failed. This procedure resulted, for all $T \leq 1400$ K, in broad frequency distributions rather than the sharp frequencies of probes on substitutional sites. We, therefore, prepared the samples by ion implantation of ^{111}In at 160 keV into pellets (thickness 0.5 mm, diameter 5 mm) of n-HfO$_2$ and n-ZrO$_2$ compacted with 0.4 GPa. The implantation was carried out at the isotope separator of HISKP/Bonn.

The first implanted sample of n-HfO$_2$, enclosed under vacuum into a fused silica tube, was used to study the annealing behavior in the PAC furnace. After implantation, the ^{111}Cd PAC spectrum showed a broad frequency distribution, similar to the ^{181}Ta spectra of the native nano-oxides. With increasing temperature, an oscillatory structure appeared. At $T \sim 1400$ K, the radioactivity was found to gather at the colder sections of the silica tube, obviously diffusing out of the sample. This differs from the observation of Luthin *et al.*[48] that pellets of coarse-grained oxides, with ^{111}In implanted with 400 keV, could be heated in air to 1643 K for hours without substantial loss of radioactivity.

Subsequently, we, therefore, annealed our samples after implantation, enclosed in fused silica tubes, in a tube furnace at only 1200 K for 10–20 h. Typical ^{111}Cd PAC spectra observed after this heat treatment are collected in Fig. 11. As much as four components with different QIs are required to reproduce the spectra over the entire temperature range. The component f_1 which dominates at all temperatures (decreasing reversibly from $f_1 \sim 0.7$ at 300 K to $f_1 \sim 0.6$ at 1200 K)
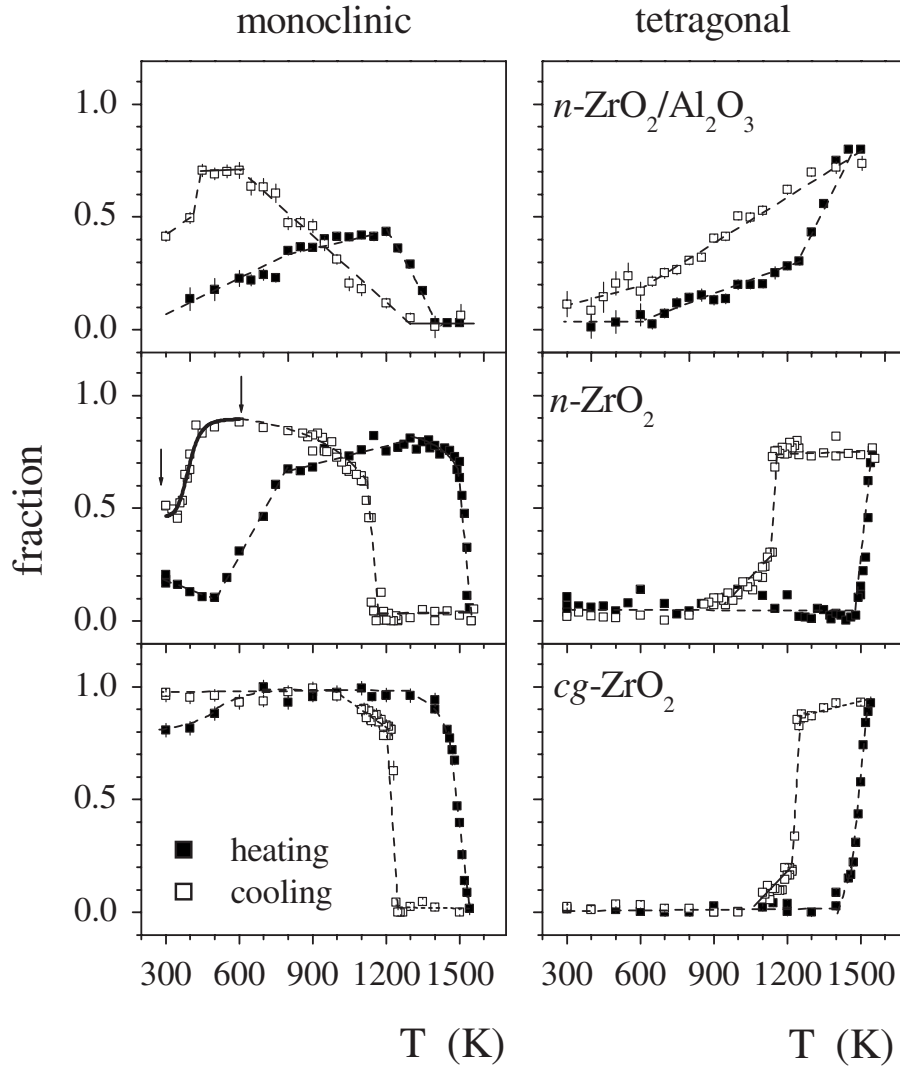
FIG. 10. The relative intensities of the monoclinic and the tetragonal phase in powder samples (in vacuum) of coated and noncoated nanoparticles of ZrO_2 and in coarse-grained ZrO_2 (from top) as a function of temperature. All samples were continuously heated to 1550 K and cooled back to 300 K. The solid line between the arrows in the middle section represents a fit of Eqs. (3) and (4) to the experimental $f_m(T)$ data measured after reaching 1550 K. The dashed lines are to guide the eye.

is characterized by a broad distribution of strong QIs. In addition, three components with sharp frequencies are found. The QI parameters of all components ($f_1 - f_4$) are listed in Table II for n-ZrO_2. The parameters of components f_2, f_3, and f_4 are very close to those observed by Luthin *et al.*,[48] the sum $\Sigma_{i=2}^{4} f_i$, however, is about a factor of 2 smaller than in the coarse-grained oxides. Component f_4 has been identified by Luthin *et al.*[48] as ^{111}Cd on substitutional sites of monoclinic ZrO_2 ($f_4 = f_m$). Components f_2 and f_3 have been associated with different charge states of oxygen neighbors of the ^{111}Cd probes caused by the trapping of electron holes. The smaller value of $\Sigma_{i=2}^{4} f_i$ suggests that in the nanoparticles, only $\sim$50% of the implanted probes end up on regular host sites, possibly because of the larger number of atoms in interfacial regions.

The relative intensities $f_4 = f_m$ of ^{111}Cd on substitutional sites of monoclinic n-ZrO_2 and n-HfO_2 [normalized to $f_m(T) \sim 1$ at $T \geqslant 1200$ K] at different temperatures are collected in Fig. 12 (full triangles), which for comparison

includes the temperature dependence of the monoclinic fraction of the probe ^{181}Ta in the same nanoparticles and of both ^{111}Cd and ^{181}Ta in the corresponding coarse-grained oxides.

It is an important observation that for the two probes of ^{181}Ta and ^{111}Cd, the temperature dependence of the monoclinic fraction $f_m(T)$ differs substantially. This indicates that probe rather than host properties must play the decisive role in the reversible appearance of nanoparticle defect components upon cooling from $T \geqslant 1200$ K. The main differences are the following:

(i) The decrease of $f_m(T)$ for the two probes extends over different temperature ranges.

(ii) In the case of ^{181}Ta, there is clear evidence for a particle size effect (see Sec. IV C 2).

(iii) In the case of ^{111}Cd, the temperature dependence of the monoclinic fraction is independent of the particle size. All ^{111}Cd probes are affected by the defect formation, both in nanocrystalline and coarse-grained oxides.
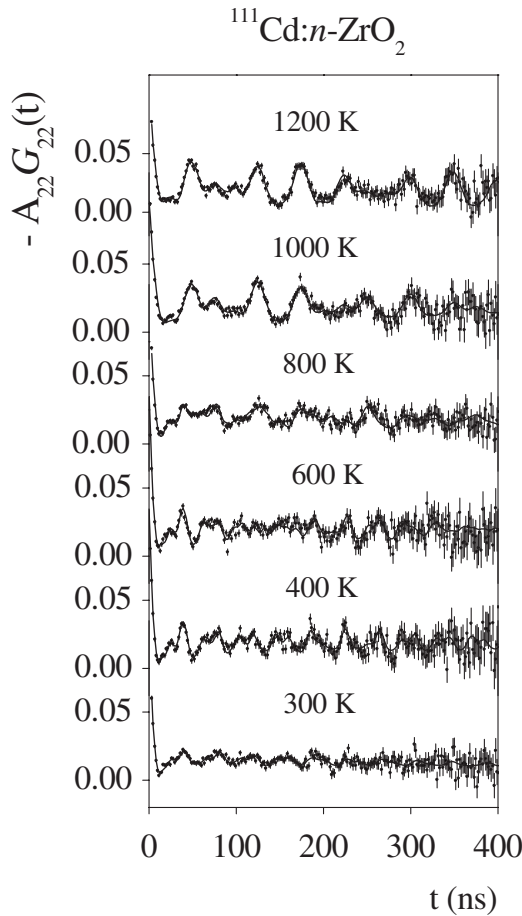
FIG. 11. PAC spectra of [111]Cd nuclei implanted into a pellet of noncoated ZrO_2 nanoparticles at different temperatures. After implantation, the pellet was annealed in vacuum at 1200 K for 20 h.

VI. DISCUSSION

A. Structural information

The PAC spectra of the nanoscaled oxides in the native state differ strongly from those of the coarse-grained material (compare the topmost spectra in Figs. 5 and 6). In the nanoparticles, the oscillations of the anisotropy typical for the bulk compounds are more or less wiped out. This attenuation of the oscillation amplitudes is clear evidence for a broad distribution of electric field gradients in the nanoparticles. As discussed in detail in Refs. 5, 6, and 44, this observation

TABLE II. The QI parameters (ν_q, η, and δ) and the relative intensities f_i of the four components present in the PAC spectra of [111]Cd in nanocrystalline ZrO_2 at 300 K.

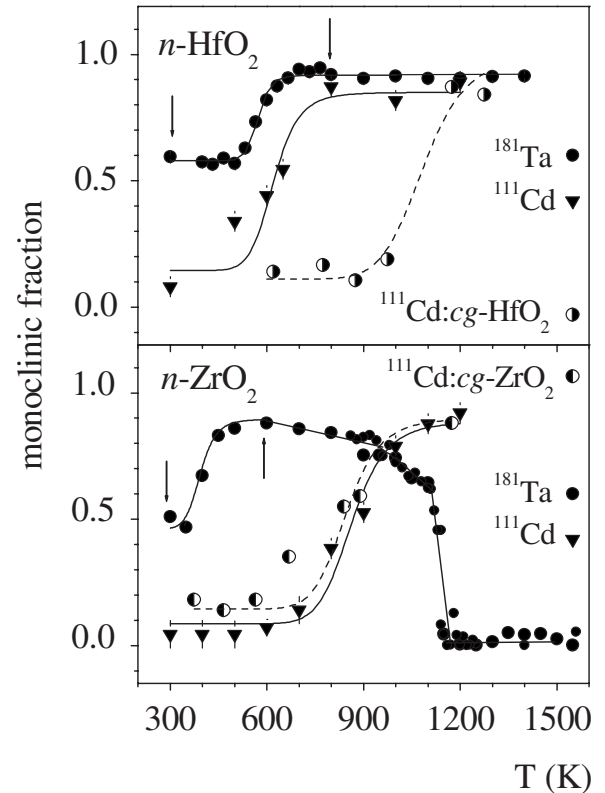| Component	Relative intensity	ν_q (MHz)	η	δ
f_1	0.7 at 300 K	150–200	0.5–0.6	0.8–0.9
f_2	0.18(2) at 400 K	166(3)	0.26(2)	0.02(1)
f_3	0.07(2) at 400 K	179(9)	0.40(2)	0.02(1)
f_4 (monoclinic)	0.4 at 1200 K	83(2)	0.55(3)	0.02(1)

FIG. 12. The fraction of the probe nuclei [181]Ta (full points) and [111]Cd (full triangles) on substitutional sites of bare monoclinic hafnia and zirconia nanoparticles as a function of temperature. The solid and dashed lines are fits of Eqs. (3) and (4) to the experimental data. The arrows mark the temperature range used in the analysis of the [181]Ta data. In the case of [111]Cd, the entire temperature range $T \leq 1200$ K was taken into account. For comparison, the fraction of [111]Cd on substitutional sites of coarse-grained (cg-) monoclinic HfO_2 and ZrO_2 (taken from Ref. 48) is included.

implies a high degree of disorder of the oxygen sublattice. Details of this oxygen disorder are difficult to infer from the QI distribution, but the oxygen vacancies detected in the XPS measurements (Sec. II B) probably play an important role. Different numbers of oxygen vacancies and distributions of the Hf-O or Zr-O distances and bond angles would lead to distributions of the QI seen by the ensemble of probe nuclei. As shown experimentally in Ref. 6 radiation damage caused by the neutron activation of the samples can be excluded.

The x-ray and electron diffraction patterns mainly reflect the structure of the cation sublattice. According to the TEM micrographs, the Hf and Zr atoms crystallize in a well-ordered, periodic structure, which has monoclinic symmetry in the case of noncoated n-HfO_2 and tetragonal or cubic symmetry in the other nanoscaled oxides. By combining the PAC and the x-ray and electron diffraction results, one may then conclude that the initial state of the HfO_2 and ZrO_2 nanoparticles investigated in this paper is characterized by a cation sublattice with well developed long-range order and a highly disordered oxygen sublattice.

With increasing temperature, the initially disordered anion sublattice transforms to an ordered structure, as shown by the

appearance of oscillations in the PAC spectra (see Fig. 6). Whereas in nanocrystalline zirconia both the monoclinic and the tetragonal phase appear, only the monoclinic phase is found in the hafnia nanoparticles. The total absence of a tetragonal component in the ^{181}Ta spectra of nanocrystalline hafnia is at variance with the XRD measurements, which suggests that samples of annealed HfO$_2$/Al$_2$O$_3$ may retain the tetragonal phase to some extent (see Fig. 3).

B. Defect complexes in HfO$_2$ and ZrO$_2$ nanoparticles

1. General considerations

It appears improbable that the appearance of the defect component in the ^{181}Ta PAC spectra reflects structural defects of the host oxides. The nanoparticles annealed at T_A ≥ 1200 K show a high degree of order; their PAC spectra are practically identical to those of the coarse-grained oxides. The formation of structural defects upon cooling would, therefore, require the diffusion of cations and/or oxygen ions. Using the diffusion parameters of oxygen in nanocrystalline zirconia determined by Brossmann *et al.*,[51] one estimates oxygen jump rates[52] of the order of $w \sim 10^{-4}$ and 10^{-1} s^{-1} for the core and the interfacial region, respectively, of nanocrystalline ZrO$_2$ at $T \sim 600$ K, where the defect component starts to appear. The cation jump rates are even smaller. We, therefore, discard—on the time scale of the PAC experiment—the possibility of atomic diffusion at $T < 700$ K and, hence, exclude structural defects as an explanation for the defect component.

Diffusionless structural transformation is also unlikely. In such a case, one would expect another static QI of possibly different symmetry and strength but narrow linewidth, and the thermal evolution of this component would not extend over a temperature range of the order of 150–200 K.

Excluding structural defects or transformations, the formation of electronic defects involving the probe atom should be considered as possible explanation of the defect component. The fact that the monoclinic fractions as seen by ^{181}Ta and ^{111}Cd, respectively, have completely different temperature dependencies $f_m(T)$ and the absence of a particle size effect in the case of ^{111}Cd (Fig. 12) point into this direction.

An important difference between these probes concerns their charge state in HfO$_2$ and ZrO$_2$. After the ^{111}In → ^{111}Cd electron capture decay, ^{111}Cd has valence 2+ and, in a lattice of tetravalent Hf or Zr ions, is attractive to positive charge carriers. Based on cluster calculations of the EFG, Luthin *et al.*[48] have attributed the observed reversible change of population f_2, $f_3 \leftrightarrow f_4$ of the components f_2, f_3, and $f_4(=f_m)$ to thermal trapping and detrapping of one or two positive electron holes at nearest oxygen neighbors of the probes. Cation vacancies are considered, by charge neutrality arguments, as the source of these electron holes.

^{181}Ta produced by the β^- decay of ^{181}Hf, on the other hand, has nominal valence 5+. Relative to tetravalent Hf and Zr, ^{181}Ta thus constitutes a positively charged impurity and it is conceivable that at low temperatures electrons are trapped by these impurity states, forming neutral Ta-electron configurations with a different QI at the nuclear site.

Casali *et al.*[53] have recently reported *ab initio* calculations

of the EFG at Ta nuclei on substitutional Hf sites of monoclinic HfO$_2$ for the Ta charge states Ta$^+$ and Ta^0. According to these calculations, the quadrupole frequency ν_q and asymmetry parameter η for charge state Ta^0 should be about 20% larger than for Ta$^+$. The difference of the experimental QI parameters of the monoclinic phase ($\nu_q \approx 800$ MHz and $\eta \approx 0.34$) and the defect component ($\nu_q \sim 1100$–1200 MHz, $\eta \sim 0.2$–0.4, and $\delta \sim 0.4$–0.6) in the nanocrystalline oxides is of this order of magnitude.

Within the framework of this interpretation, the pronounced line broadening of the defect component—attributable to either a static QI distribution or slow QI fluctuations (see Sec. IV C 2)—requires the existence of several trapping sites. A static occupation of nonequivalent sites would produce a QI distribution; electrons slowly hopping between equivalent sites would lead to QI fluctuations.

2. ^{181}Ta impurities as electron traps in n-HfO$_2$ and n-ZrO$_2$: A two-state model

The proposed electron trapping can be described in a two-state model where mobile electrons are either in the conduction band at $E \equiv 0$ or occupy the Ta$^+$ states at $-E_d$. The relative intensity of the defect component in thermal equilibrium, i.e., the fraction of probe nuclei decorated with a trapped electron, is then given by [Maxwell–Boltzmann distribution with degeneracies c_P and $(1-c_P)$, c_P=relative probe concentration]

$$f_d(T) = f_0 \frac{1}{[1 + (1/c_P - 1)\exp(-E_d/k_B T)]} \quad (3)$$

with $f_0 = 1$ for $c_e \geq c_p$, and $f_0 = c_e/c_p$ for $c_e < c_p$, where c_p and c_e are the probe and electron concentrations, respectively. The fraction $f_m(T)$ of probes in the monoclinic phase without a trapped electron is then

$$f_m(T) = [1 - f_V f_d(T)]. \quad (4)$$

The parameter f_V is a measure of the volume fraction where electrons are available for trapping.

Fits of Eqs. (3) and (4) to the $f_m(T)$ data of ^{181}Ta in Figs. 8–10 lead to Ta-electron binding energies of $E_d \sim 0.90(15)$ eV and $E_d \sim 0.6(1)$ eV for nanocrystalline hafnia and zirconia (similar values for bare and Al$_2$O$_3$-coated particles), respectively, and a probe concentration ratio c_p (probes per total number of metal ions) between 10^{-6} and 10^{-8}. The relatively large uncertainties of c_p and E_d are a consequence of the strong correlation of these parameters in Eq. (3). Assuming that the number of mobile electrons available exceeds the number of probes ($c_e \geq c_p$, i.e., $f_0 = 1$), one obtains $f_V \sim 0.35$–0.4.

The value of c_p deduced from $f_m(T)$ in Figs. 8–10 is in good agreement with the probe concentration estimated from the γ-ray intensity of the PAC source. The total number of ^{181}Ta probes of a typical PAC source is of the order of 10^{12} atoms which, for oxide samples of a few milligrams, correspond to a probe concentration $c_p \sim 10^{-7}$.

The proposed interpretation of the defects as Ta probes with a trapped electron requires a total of 10^{11}–10^{12} mobile electrons. One possible electron source are positively

charged oxygen vacancies. To account for the experimentally observed size effect ($f_V \sim 0.35$–0.4 at grain diameter $d \sim 25$–30 nm, and $f_V \sim 0$ at $d > 100$ nm), these would have to be concentrated—in the case of a spherical particle—in a surface layer of ~ 3.5 nm thickness. A conceivable mechanism for such concentration has been mentioned by Shukla and Seal[30] in a discussion of the "nanoparticle size effect": In nanocrystalline powders with an important fraction of the atoms residing near the surface, a large number of metal-oxygen bonds may be weakened, resulting in the desorption of oxygen ions and the creation of oxygen vacancies in the surface region.

A concentration of oxygen vacancies in the grain boundaries is experimentally supported by our XPS results, by the enhanced oxygen diffusion[51] in the grain boundaries of n-ZrO$_2$, and by EXAFS studies[19] of nanocrystalline ZrO$_2$.

In high-temperature PAC spectra of ^{181}Ta in zirconia with a large number of oxygen vacancies, one usually observes nuclear spin relaxation effects caused by rapidly diffusing oxygen. Examples are the PAC investigations by Gardner *et al.*[54] and Rivas *et al.*[55] of Y-stabilized ZrO$_2$ (YSZ), where the substitution of tetravalent Zr by trivalent Y leads to a large number of vacant oxygen sites. In YSZ with 16.9 at. % Y$_2$O$_3$ at 1000 K, e.g., the dynamic QI induces an exponential decay of the anisotropy with decay constant $\lambda_2 \sim 200$ MHz. The absence of such dynamic effects in the high-temperature spectra of the nano-oxides ($\lambda_2 < 4$ MHz) does not argue against the proposed defect model because of the low vacancy concentration ($\leq 10^{-12}$) required.

Kang *et al.*[24] have shown that defect complexes consisting of oxygen vacancies and hydrogen (V_O-H) behave as shallow donors. Such complexes probably exist in the surface region of the nanoparticles. The ^{1}H-MAS NMR have established that after heating to high temperatures, their hydrogen concentration is still in the range of 2.5–5.0 wt% (see Sec. II B). Even after 60 h at 1500 K, as much as 0.15 wt % of H was detected. It may, hence, be assumed that the nanoparticles of the encapsulated PAC sources still carry a sizable hydrate layer when they are cooled from high temperatures. V_O-H complexes at the interface of nanoparticles and their hydrate layers may, therefore, constitute another possible source of the electrons required by the Ta$^+$ trapping model.

Although the reduction of the monoclinic fraction is not affected by the hydrogen concentration, there are indications that hydrogen has some influence: Expelling the hydrogen to a large extent leads to the reversible appearance of an additional, high frequency component in the PAC spectra (See Sec. IV C 2). For an understanding of these observations and a full assessment of the importance of the hydrate layer, further experimental studies appear necessary.

The trapping model provides a qualitative description of the temperature dependence of the different fractions observed in the PAC spectra of ^{181}Ta in nanocrystalline HfO$_2$ and ZrO$_2$. In the frame of this model, the appearance of the defect component suggests the existence of a Ta$^+$ impurity state at about $E_d \sim 0.90(15)$ eV and $E_d \sim 0.6(1)$ eV below the conduction band of n-HfO$_2$ and n-ZrO$_2$, respectively, which may be occupied by electrons provided by oxygen vacancies and/or shallow H donors in the interfacial region of the nano-

particles. PAC measurements of nanocrystalline hafnia doped with a few atomic percent of nonradioactive Ta could possibly help to corroborate the proposed interpretation of the defect component. Such experiments are presently in preparation.

It is noteworthy that upon heating, the disordered component II in the PAC spectra of the coarse-grained material vanishes, irreversibly, in the same temperature range as the reversible defect component of the nanocrystalline oxides (see Figs. 8 and 10), which—together with the similarity of their QI parameters—suggests that in both cases one observes the dissolution of the same defect. As indicated by the XRD pattern of cg-ZrO$_2$ in the bottommost section of Fig. 4, coarse-grained oxides may contain some disorder in the native state and a certain fraction of neutral Ta-electron complexes is possibly formed. Upon heating, these complexes become ionized and the disordered fraction vanishes. However, with increasing temperature, the oxygen vacancies also migrate toward grain-boundary sinks and, as the fraction of Ta probes in the grain-boundary volume of coarse-grained particles is very small, the disordered component in the PAC spectra of cg-ZrO$_2$ and cg-HfO$_2$ does not reappear upon cooling.

The same trapping model involving positive electron holes rather than electrons may be used to describe the reversible temperature dependence of the monoclinic fraction of ^{111}Cd^{2+} in nanocrystalline and coarse-grained[48] HfO$_2$ and ZrO$_2$ (see Fig. 12). In contrast to ^{181}Ta, in the case of ^{111}Cd, the monoclinic fraction—both in bulk and nanocrystalline oxides—disappears completely upon cooling [volume fraction in Eq. (4), $f_V = 1$]. This absence of a size effect means that all probe atoms participate in hole trapping and detrapping, and implies a homogeneous distribution of electron holes throughout the samples.

A fit of Eqs. (3) and (4) to the $f_m(T)$ data of ZrO$_2$ in Fig. 12, assuming $f_V = 1$ and probe concentrations in the range $c_p = 10^{-6}$–10^{-8}, results in a Cd-electron hole binding energy of $E_d = 1.15(15)$ eV both for nanocrystalline and coarse-grained ZrO$_2$ particles. [Note: Although two defect configurations (f_2, f_3) are involved, the use of Eq. (3) in the analysis of $f_m(T)$ is justified since both defects feed the monoclinic fraction f_m with about the same binding energy as shown in the temperature dependencies $f_2(T)$ and $f_3(T)$ in Ref. 48.] For HfO$_2$, the data presently available suggest an influence of the particle size on the binding energy: For ^{111}Cd in bulk and nanocrystalline HfO$_2$, one obtains $E_d = 1.5(2)$ eV and $E_d \leq 0.85(2)$, respectively.

VII. SUMMARY

X-ray and electron diffraction (TEM) has been combined with PAC measurements of nuclear electric QIs to investigate structure, phase transformations, and grain growth of hafnia and zirconia nanoparticles. Bare and alumina-coated nanocrystalline HfO$_2$ and ZrO$_2$ were produced by a microwave-plasma process. This route of synthesis leads to a narrow size distribution with an average diameter of ~ 3–5 nm. The native state was chemically characterized by XPS, ^{1}H MAS NMR, and thermogravimetric and combus-

tion analysis. The oxygen-metal ratio, determined by XPS to be in the range $1.4 \leqslant x \leqslant 1.8$, indicates a high concentration of oxygen vacancies. A hydrate surface layer with a hydrogen content of 5–10 wt %, consisting of chemisorbed hydroxyl groups and organic precursor fragments, was detected by ^{1}H-MAS NMR. Heating experiments showed that temperatures $T \gtrsim 1500$ K are required to completely expel the hydrogen from the plasma-synthesized particles.

From the x-ray and electron diffraction patterns, we conclude that native zirconia nanoparticles crystallize in the cubic or tetragonal phase. Upon annealing, the monoclinic phase appears at a critical particle diameter $d_{cr} \sim 20$ nm. The critical particle diameter for the tetragonal-to-monoclinic transformation of n-HfO$_2$ is $d_{cr} \lesssim 5.5$ nm. In contrast to n-ZrO$_2$, bare HfO$_2$ nanoparticles are, therefore, synthesized in the monoclinic phase. When the nanoparticles are coated with a layer of Al$_2$O$_3$, the stress caused by the volume expansion of the $t \rightarrow m$ transition in the Al$_2$O$_3$ confined particles favors the tetragonal over the monoclinic phase both in hafnia and zirconia nanoparticles. The Al$_2$O$_3$ coating also obstructs the growth of the hafnia and zirconia cores. The grain growth enthalpy Q_A of bare n-ZrO$_2$ has been determined from the decrease of the XRD linewidth upon annealing. The result $Q_A = 32(5)$ kJ/mole, both for the monoclinic and the tetragonal phase, is comparable to the values reported for most other routes of synthesis.

The QI of the nuclei [181]Ta and [111]Cd on metal sites of bare and Al$_2$O$_3$-coated HfO$_2$ and ZrO$_2$ nanoparticles has been determined by PAC spectroscopy as a function of temperature. For comparison, the QI of [181]Ta in commercial coarse-grained oxides has been studied in the same temperature range 300 K $\leqslant T \leqslant$ 1550 K. The room temperature [181]Ta PAC spectra of the native nanocrystalline particles reflect a broad distribution of QIs, which is evidence for a high degree of disorder of the oxygen sublattice. Together, the TEM and the PAC results describe the nanoparticles as oxides with a fairly well developed long-range order of the cation sublattice and a strong disorder of the anion sublattice.

Upon heating, particle growth and ordering of the oxygen sublattice set in and the PAC spectra of the nanoparticles evolve toward those of the coarse-grained oxides. In n-HfO$_2$, only the monoclinic phase is observed up to $T \leqslant 1450$ K. While bare n-ZrO$_2$ presents a sharp $m \rightarrow t$ transition with a hysteresis of about 200 K, in coated n-ZrO$_2$/Al$_2$O$_3$, the monoclinic and the tetragonal phase coexist over a temperature range of almost 1000 K.

A defect component involving $\sim 30\% - 40\%$ of the probe nuclei appears in the [181]Ta PAC spectra at temperatures $T < 700$ K when well crystallized nanoparticles are cooled from $T \gtrsim 1200$ K. The reversible temperature dependence of the intensity of this component can be reproduced by a trapping model which assumes that Ta impurities in hafnia and zirconia may trap electrons at low temperatures. The fact that the defect component appears only in particles with diameter $d < 100$ nm suggests that mobile electrons are available only in the surface region of the oxide particles, either from oxygen vacancies (V_O) and/or V_O-hydrogen donors at the interface of the nanoparticles and their hydrate layers. This conclusion is supported by the absence of a size effect for [111]Cd probes in HfO$_2$ and ZrO$_2$. The temperature dependence of the [181]Ta defect fraction is consistent with a Ta$^+$ impurity level at $E_d \sim 0.9$ and 0.6 eV below the hafnia and zirconia conduction bands, respectively.

*Corresponding author; forker@iskp.uni-bonn.de

†Present address: Instituto de Magnetismo Aplicado, P.O. Box 155, 28230 Las Rozas, Madrid, Spain.

[1] J. M. Ramallo López, M. Rentería, E. E. Miró, F. G. Requejo, and A. Traverse, Phys. Rev. Lett. **91**, 108304 (2003).

[2] B. Bai and G. S. Collins, Hyperfine Interact. **79**, 761 (1993).

[3] H. Wolf, H. G. Zimmer, T. Fitz, and Th. Wichert, Nanostruct. Mater. **6**, 613 (1995).

[4] Th. Agne, Z. Guan, X. M. Li, H. Wolf, Th. Wichert, H. Natter, and R. Hempelmann, Appl. Phys. Lett. **83**, 1204 (2003).

[5] M. Forker, U. Brossmann, and R. Würschum, Phys. Rev. B **57**, 5177 (1998).

[6] M. Forker, J. Schmidberger, D. V. Szabó, and D. Vollath, Phys. Rev. B **61**, 1014 (2000).

[7] A. S. Foster, F. Lopez Gejo, A. L. Shluger, and R. M. Nieminen, Phys. Rev. B **65**, 174117 (2002).

[8] A. S. Foster, V. B. Sulimov, F. Lopez Gejo, A. L. Shluger, and R. M. Nieminen, Phys. Rev. B **64**, 224108 (2001).

[9] K. Xiong, J. Robertson, M. C. Gibson, and S. J. Clark, Appl. Phys. Lett. **87**, 183505 (2005).

[10] J. Robertson, Rep. Prog. Phys. **69**, 327 (2006).

[11] A. Ayala, R. Alonso, and A. López-Garcia, Phys. Rev. B **50**, 3547 (1994).

[12] H. Jaeger, J. A. Gardner, J. C. Haygarth, and R. L. Rasera, J. Am. Ceram. Soc. **69**, 458 (1986).

[13] D. Vollath, M. Forker, M. Hagelstein, and D. V. Szabó, MRS Symposia Proceedings No. 634 (Materials Research Society, Pittsburgh, 2001), p. B7.7.1.

[14] D. Vollath and K. E. Sickafus, Nanostruct. Mater. **1**, 427 (1992); J. Mater. Res. **8**, 2978 (1993).

[15] D. Vollath and D. V. Szabó, Nanostruct. Mater. **4**, 927 (1994).

[16] D. Vollath and D. V. Szabó, in *Innovative Processing of Films and Nanocrystalline Powders*, edited by K. L. Choy (Imperial College Press, London, 2002).

[17] R. Hesse, UNIFIT for Windows, University of Leipzig, Germany, 2006.

[18] J. H. Scofield, J. Electron Spectrosc. Relat. Phenom. **8**, 129 (1976).

[19] M. Winterer, R. Nitsche, and H. Hahn, Nanostruct. Mater. **9**, 397 (1997).

[20] M. Hagelstein, H. O. Moser, D. Vollath, C. Ferrero, and M. Borowski, J. Synchrotron Radiat. **8**, 522 (2001).

[21] H. Liu, L. Feng, X. Zhang, and Q. Xue, J. Phys. Chem. **99**,.332 (1995).

[22] D. G. Cory and W. M. Ritchey, J. Magn. Reson. (1969-1992) **80**, 128–132 (1988).

[23] A. V. Chadwick, G. Mountjoy, V. M. Nield, I. J. F. Poplett, M. E. Smith, J. H. Strange, and M. G. Tucker, Chem. Mater. **13**, 1219 (2001).

[24] J. Kang, E.-C. Lee, K. J. Chang, and Y. G. Jin, Appl. Phys. Lett. **84**, 3894 (2004).

[25] H. P. Klug and L. E. Alexander, *X-Ray Diffraction Procedures* (Wiley, New York, 1974).

[26] JCPDS-International Centre for Diffraction Data, ICDD Card Nos. 08-0342 (t-HfO2) and 43-1017 (m-HfO2).

[27] I. A. El-Shanshoury, V. A. Rudenko, and I. A. Ibrahim., J. Am. Ceram. Soc. **53**, 264 (1970).

[28] D. Vollath, F. D. Fischer, M. Hagelstein, and D. V. Szabó, J. Nanopart. Res. **8**, 1003 (2006).

[29] R. G. Garvie, J. Phys. Chem. **82**, 218 (1978).

[30] S. Shukla and S. Seal, Int. Mater. Rev. **50**, 4 (2005).

[31] S. V. Ushakov, A. Navrotsky, Y. Yang, S. Stemmer, K. Kukli, M. Ritala, M. A. Leskelä, P. Fejes, A. Demkov, C. Wang, B.-Y. Nguyen, D. Triyoso, and P. Tobin, Phys. Status Solidi B **241**, 2268 (2004).

[32] V. F. Petrunin, V. V. Popov, H. Z. Zhu, and S. A. Korovin, Glass Phys. Chem. **31**, 459 (2005).

[33] T. Chraska, A. H. King, and C. B. Berndt, Mater. Sci. Eng., A **286**, 169 (2000).

[34] G. Gou and Y. Chen, J. Solid State Chem. **178**, 1675 (2005).

[35] J. A. Eastman, J. Appl. Phys. **75**, 770 (1994).

[36] Y. Xiong, K. N. Yu, and C. Xiong, Phys. Rev. B **49**, 5607 (1994).

[37] G. G. Siu, M. J. Stokes, and Y. Liu, Phys. Rev. B **59**, 3173 (1999).

[38] B. L. Kirsch, A. E. Riley, A. F. Gross, and S. H. Tolbert, Langmuir **20**, 11247 (2004).

[39] G. Baldinozzi, D. Simeone, D. Gosset, and M. Dutheil, Phys. Rev. Lett. **90**, 216103 (2003).

[40] R. Würschum, G. Soyez, and H.-E. Schaefer, Nanostruct. Mater. **3**, 225 (1993).

[41] M. Forker, W. Herz, U. Hütten, M. Müller, R. Müsseler, J. Schmidberger, D. Simon, A. Weingarten, and S. C. Bedi, Nucl. Instrum. Methods Phys. Res. A **327**, 456 (1993).

[42] H. Frauenfelder and R. M. Steffen, in *Perturbed Angular Correlations*, edited by K. Karlsson, E. Matthias, and K. Siegbahn (North Holland, Amsterdam, 1963).

[43] G. Schatz and A. Weidinger, *Nuclear Solid State Physics* (Wiley, New York, 1996).

[44] S. Schlabach, D. V. Szabó, D. Vollath, P. de la Presa, and M. Forker, J. Appl. Phys. **100**, 024305 (2006).

[45] H. Saitovitch, P. R. J. Silva, A. F. Pasquevich, and M. Forker (private communication).

[46] H. Winkler and E. Gerdau, Z. Phys. **262**, 363 (1973).

[47] A. Baudry and P. Boyer, Hyperfine Interact. **35**, 803 (1987).

[48] J. Luthin, K. P. Lieb, M. Neubauer, M. Uhrmacher, and B. Lindgren, Phys. Rev. B **57**, 15272 (1998).

[49] R. Wang, J. A. Gardner, W. E. Evenson, and J. A. Sommers, Phys. Rev. B **47**, 638 (1993).

[50] N. Mommer, Th. Lee, J. A. Gardner, and W. E. Evenson, Phys. Rev. B **61**, 162 (2000).

[51] U. Brossmann, R. Würschum, U. Södervall, and H.-E. Schaefer, J. Appl. Phys. **85**, 7646 (1999).

[52] P. Heitjans and S. Indris, J. Phys.: Condens. Matter **15**, R1257 (2003).

[53] R. A. Casali and M. A. Caravaca, Solid State Commun. **134**, 413 (2005).

[54] J. A. Gardner, H. Jaeger, H. T. Su, W. H. Warnes, and J. C. Haygarth, Physica B **150**, 223 (1988).

[55] P. C. Rivas, M. C. Caracoche, A. F. Pasquevich, J. A. Martínez, A. M. Rodriguez, A. R. López-Garcia, and S. R. Mintzer, J. Am. Ceram. Soc. **79**, 831 (1996).